Article

Lysine-arginine imbalance overcomes therapeutic tolerance governed by the transcription factor E3-lysosome axis in glioblastoma

Yongwei Jing [1,12], Masahiko Kobayashi[1,12], Mahmoud I. Shoulkamy [2,3], Meiqi Zhou[1], Ha Thi Vu [1,11], Hiroshi Arakawa [4], Hemragul Sabit[5], Sadahiro Iwabuchi [6], Cong Quang Vu [2], Atsuko Kasahara[1,2,7], Masaya Ueno [1,2], Yuko Tadokoro[1,2], Kenta Kurayoshi[1], Xi Chen[1], Yuhang Yan[1], Satoshi Arai [2], Shinichi Hashimoto [6], Tomoyoshi Soga [8,9], Tomoki Todo[10], Mitsutoshi Nakada [5] & Atsushi Hirao [1,2] ✉

Recent advances in cancer therapy have underscored the importance of targeting specific metabolic pathways. In this study, we propose a precision nutrition approach aimed at lysosomal function in glioblastoma multiforme (GBM). Using patient-derived GBM cells, we identify lysosomal activity as a unique metabolic biomarker of tumorigenesis, controlling the efficacy of temozolomide (TMZ), a standard GBM therapy. Employing combined analyses of clinical patient samples and xenograft models, we further elucidate the pivotal role of Transcription Factor Binding To IGHM Enhancer 3 (TFE3), a master regulator of lysosomal biogenesis, in modulating malignant properties, particularly TMZ tolerance, by regulating peroxisome proliferator-activated receptor-gamma coactivator 1–alpha (PGC1α)-mediated mitochondrial activity. Notably, we find that lysine protects GBM cells from lysosomal stress by counteracting arginine's effects on nitric oxide production. The lysine restriction mimetic, homoarginine administration, significantly enhances the efficacy of anticancer therapies through lysosomal dysfunction. This study underscores the critical role of lysosomal function modulated by amino acid metabolism in GBM pathogenesis and treatment.

Precise regulation of metabolic processes is essential for tissue homeostasis[1]. Recent research has increasingly focused on understanding how nutrient-driven metabolism influences the malignancy of cancer cells[2,3]. While metabolic regulation has long been recognized as critical for cellular adaptation to environmental changes, recent studies highlight the direct impact of metabolic organelle dynamics on cell fate determination[4,5]. Specific organelles play pivotal roles in cancer initiation and progression due to their involvement in energy homeostasis and cell death[6]. In particular, mitochondrial metabolism contributes to malignant transformation through mechanisms involving mitochondrial reactive oxygen species (ROS) and the abnormal accumulation of specific mitochondrial metabolites like fumarate, succinate, and 2-hydroxyglutarate (2-HG)[7,8]. As a result, mitochondrial metabolism emerges as a promising target for the development of antitumor agents. Therefore, organelle-targeted therapies have been explored to enhance the efficacy of therapeutic agents.

The lysosome is an acidic and dynamic membrane-bound organelle, which contains over 50 different hydrolytic enzymes and serves as a cellular digestive center in which intra- and extracellular components are degraded[9]. This process involves the fusion of lysosomes with autophagosomes or endosomes and is required for the quality control of cellular components and the recycling of materials[10]. Lysosomes serve as signaling hubs, which are essential for amino acid sensing, metabolic signal transduction, and autophagy regulation[11]. Additionally, lysosomes interact with other intracellular organelles, such as mitochondria and the endoplasmic reticulum, to control energy homeostasis[12,13]. Recent studies have shown that lysosomes may play important roles in cancer development and progression via their involvement in the abovementioned biological processes. Mechanistically, alterations in metabolic signaling, mediated by the transcription factor EB (TFEB)-mTORC1 axis affect cancer malignancy[14]. For instance, while MiT/TFE family members such as TFEB and TFE3 regulate lysosomal biogenesis via the transcriptional network, they also promote metabolic reprogramming and malignancy in pancreatic cancer[15]. *TFEB* overexpression has been shown to promote prostate cancer progression via a mechanism involving lysosomal biogenesis[16]. The microphthalmia-associated transcription factor (MITF), which is also a member of the MiT/TFE family, was recognized as a master regulator in melanocytes and a major melanoma oncogene, which is amplified in 30%–40% of melanomas and determines their proliferative or invasive phenotypes[17].

Glioblastoma (GBM) stands as the most prevalent and deadliest brain tumor. Traditional treatment for GBM involves surgery, temozolomide (TMZ), and radiation, forming the cornerstone of therapeutic approaches[18]. While TMZ effectively triggers GBM cell death in many cases, a substantial portion of patients exhibit resistance to this treatment[19]. One typical reason for TMZ resistance is the activation of O^6-methylguanine-DNA methyl-transferase (MGMT), an endogenous DNA repair enzyme vital for maintaining genomic integrity[19,20]. In addition, dysregulation in specific molecular pathways, such as the PI3K/AKT pathway, RTK aberrations, JAK/STAT pathway, and autophagy, has been associated with the efficacy of TMZ[21]. Recent research has revealed the elevated levels of metabolites, including glucose, citrate, and isocitrate, in TMZ-resistant GBM cells[22], suggesting a close relationship between metabolic reprogramming and TMZ resistance in GBM.

In this current study, we unveil the critical role of the TFE3-lysosome axis for regulating drug tolerance and highlight the crucial role of lysine as an essential amino acid in lysosomal function. Recent research has revealed that lysine catabolism influences antitumor immunity through the crotonyl-coenzyme A (crotonyl-CoA) pathway in GBM cells[23]. In addition to this pathway, our study demonstrates that lysine plays a significant role in the promotion of TFE3-mediated malignant properties of GBM mediated by maintaining lysosomal function. Moreover, we have successfully developed a lysosome-targeting therapeutic strategy by manipulating the lysine-arginine balance, which we combined with TMZ. As a result, we propose a precision nutrition approach, centered around amino acid metabolism modulation, as a promising avenue for the treatment of malignant glioma.

Results

Lysosomal activity is a metabolic biomarker of tumorigenesis in GBM

Lysosomes play pivotal roles in the development and progression of cancer, closely intertwined with cancer cell proliferation, energy metabolism, invasion, metastasis, immune evasion, and angiogenesis[24]. Consequently, we embarked on an investigation to determine whether lysosomal activity could serve as a biomarker for the malignant status in glioblastoma (GBM). We assessed lysosomal proteolytic activity in various patient-derived GBM cell lines cultured in spheroids using the DQ-BSA assay, which detects fluorescent signals upon lysosomal proteolytic enzyme-mediated substrate degradation. Our findings revealed that most patient-derived GBM cell lines exhibited higher lysosomal activities compared with immortalized human neural progenitor cells derived from embryonic brain tissue, with some variation among the cell lines (Fig. 1A). To understand how lysosomal proteolytic activity impacted the biology of the GBM, we conducted spheroid culture assays in semi-solid media, focusing on sphere-forming ability. Notably, we observed a positive correlation between lysosomal proteolytic activity and sphere size (Fig. 1B), even though the number of spheres varied among the GBM cell lines. To further explore the relationship between lysosomal proteolytic activity and GBM cell phenotypes, we categorized six GBM cell lines into two groups based on lysosomal proteolytic activity: Lyso-high (KGS10, KGS23, and TGS04) and Lyso-low (KGS03, KGS04, and KGS22). We assessed lysosomal activity by measuring cathepsin B activity and lysosomal pH, using the Rhodamine 110 cathepsin B substrate and a ratiometric pH detection method with pHLys Red and LysoPrime Green, respectively. Compared with Lyso-low GBM cells, Lyso-high GBM cells exhibited increased cathepsin B-dependent proteolytic activity, a more acidic lysosomal environment, and smaller lysosomal size, indicating enhanced lysosomal function (Fig. 1C, D, Supplementary Fig. 1A). L-Leucyl-L-Leucine methyl ester (LLOMe), a reagent promoting lysosomal membrane permeabilization (LMP), induced more pronounced galectin-3 punctation in the Lyso-low GBM cells compared with the Lyso-high GBM cells (Fig. 1E, Supplementary Fig. 1B). While cathepsin C influences LLOMe cleavage and oligomerization to form a potent detergent, cathepsin C levels were comparable between Lyso-high and Lyso-low GBM cells (Supplementary Fig. 1C). Given that the lysosomal pH of Lyso-high GBM cell lines was lower than that of Lyso-low cell lines (Fig. 1D), we assume that greater lysosomal acidity increases LLOMe's effects on the lysosomal membrane in Lyso-high GBM cells. The levels of LMP, indicated by galectin-3 punctation induced by LLOMe, were lower in Lyso-high GBM cell lines compared to Lyso-low cell lines, suggesting that Lyso-high GBM cells exhibit reduced sensitivity to lysosomal damage. Subsequently, we performed molecular characterization across the Lyso-high and Lyso-low GBM cells by RNA-sequencing analysis. Gene set enrichment analysis (GSEA) of RNA-sequencing data from these cell lines revealed upregulation of signaling targets indicative of malignancy, such as Myc, mTOR, and E2F, in the Lyso-high group (Fig. 1F, Supplementary Fig. 1D–F). Additionally, gene signatures associated with mitochondrial activity, including components of the electron transport chain, oxidative phosphorylation, and amino acid metabolism, were significantly upregulated in the Lyso-high group (Supplementary Fig. 1G–K). Consistent with gene expression profiles, the Lyso-high group displayed increased mitochondrial membrane potential and mitochondrial ROS compared with the Lyso-low group (Fig. 1G, H).

Additionally, because the gene ontology analysis revealed an enrichment of calcium-regulated biological process in Lyso-high GBM cell lines, (Supplementary Fig. 1L), we compared calcium levels between cell populations with high (highest 15%) and low (lowest 15%) lysosomal proteolytic activity based on DQ-BSA staining. The comparison revealed that cells with high lysosomal proteolytic activity had higher calcium levels than cells with low lysosomal proteolytic activity (Supplementary Fig. 1M, N). Because treatment of GBM cells with a calcium chelator, BAPTA, clearly suppressed lysosomal proteolytic activity, intracellular calcium is considered a critical regulator of lysosomal proteolytic activity in GBM cells (Supplementary Fig. 1O). To investigate the in vivo relevance, we orthotopically transplanted luciferase-labeled GBM cells into immunocompromised mice. The data suggested that GBM cells from the Lyso-high group exhibited faster growth, as indicated by bioluminescence intensity (Fig. 1I). Moreover, mice implanted with Lyso-high cells had significantly shorter survival periods compared with those mice receiving transplantation of
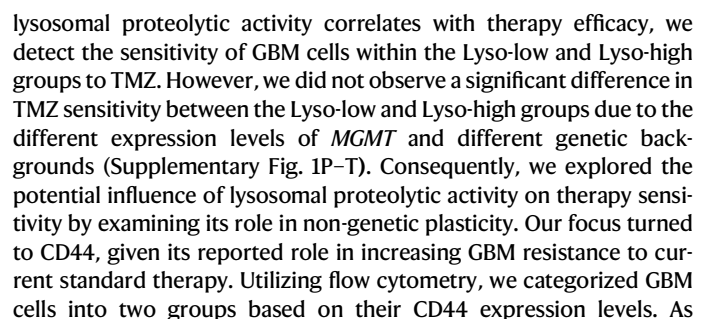
Lyso-low cells (Fig. 1J). The bioluminescence signal originating from tumors was observed in mice that exhibited prolonged survival (Fig. 1I), therefore, the in vivo proliferation of GBM cells differed between the Lyso-high and Lyso-low groups, but not due to variations in the success rate of transplantation. These results underscore the critical role of lysosomal activity as a metabolic biomarker for GBM tumorigenesis and malignancy.

Lysosomal proteolytic activity determines therapeutic efficacy

One of the primary factors contributing to the malignancy of gliomas is inherent resistance to conventional therapy. To investigate whether

lysosomal proteolytic activity correlates with therapy efficacy, we detect the sensitivity of GBM cells within the Lyso-low and Lyso-high groups to TMZ. However, we did not observe a significant difference in TMZ sensitivity between the Lyso-low and Lyso-high groups due to the different expression levels of *MGMT* and different genetic backgrounds (Supplementary Fig. 1P–T). Consequently, we explored the potential influence of lysosomal proteolytic activity on therapy sensitivity by examining its role in non-genetic plasticity. Our focus turned to CD44, given its reported role in increasing GBM resistance to current standard therapy. Utilizing flow cytometry, we categorized GBM cells into two groups based on their CD44 expression levels. As

Fig. 1 | Lysosomal activity is associated with the malignant phenotype of GBM.
A Detection of lysosomal proteolytic activity at the basal level with DQ-BSA in patient-derived GBM cell lines with confocal fluorescence microscopy ($n = 30$ cells/group). NPC, human neural progenitor cells. **B** The correlation analysis of the average sphere size formed in a medium containing 1% methylcellulose for 10 days and lysosomal proteolytic activity from A in GBM cell lines. Red: Lyso-high; Black: Lyso-low GBM cell lines ($n = 3$ independent experiments). **C** Detection of cathepsin B activity at the basal level in Lyso-high (red line) and Lyso-low (black line) GBM cell lines using flow cytometry ($n = 3$ independent experiments). **D** Measurement of lysosomal pH at the basal level in Lyso-high (red line) and Lyso-low (black line) GBM cell lines using flow cytometry ($n = 3$ independent experiments). **E** The representative images and quantification of galectin-3 punctation in GBM cells treated with 50 μM LLOMe for 15 min ($n = 3$ independent experiments). Scale bars, 10 μm. **F** GSEA results of RNA-seq data in the

Lyso-high versus Lyso-low GBM cells. FDR < 25%. **G, H** Mitochondrial membrane potential (**G**) and mitochondrial ROS (**H**) at the basal level were detected with JC-10 and MitoSOX, respectively, and evaluated in Lyso-high (red line) and Lyso-low (black line) GBM cell lines ($n = 3$ independent experiments). **I** Representative bioluminescence images of mice bearing GBM cells after 6 and 27 weeks after transplantation ($n = 3$ mice/GBM cell line). **J** Kaplan–Meier survival curves for nude mice transplanted with Lyso-high (red) or Lyso-low (black) GBM cells ($n = 3$ mice/GBM cell line). Data are presented as the means ± SD. Statistical analysis (**A, C, G**, and **H**) using unpaired two-tailed Student's t-tests. Statistical analysis (**B**) using Pearson correlation analysis. Statistical analysis (**D**) using two-tailed nested t-test. Statistical analysis (**E**) using one-way ANOVA. Statistical analysis (**J**) using Kaplan–Meier method with the log-rank test. ****$p < 0.0001$. Experiments were repeated at least three times with similar results. Source data are provided with this paper.
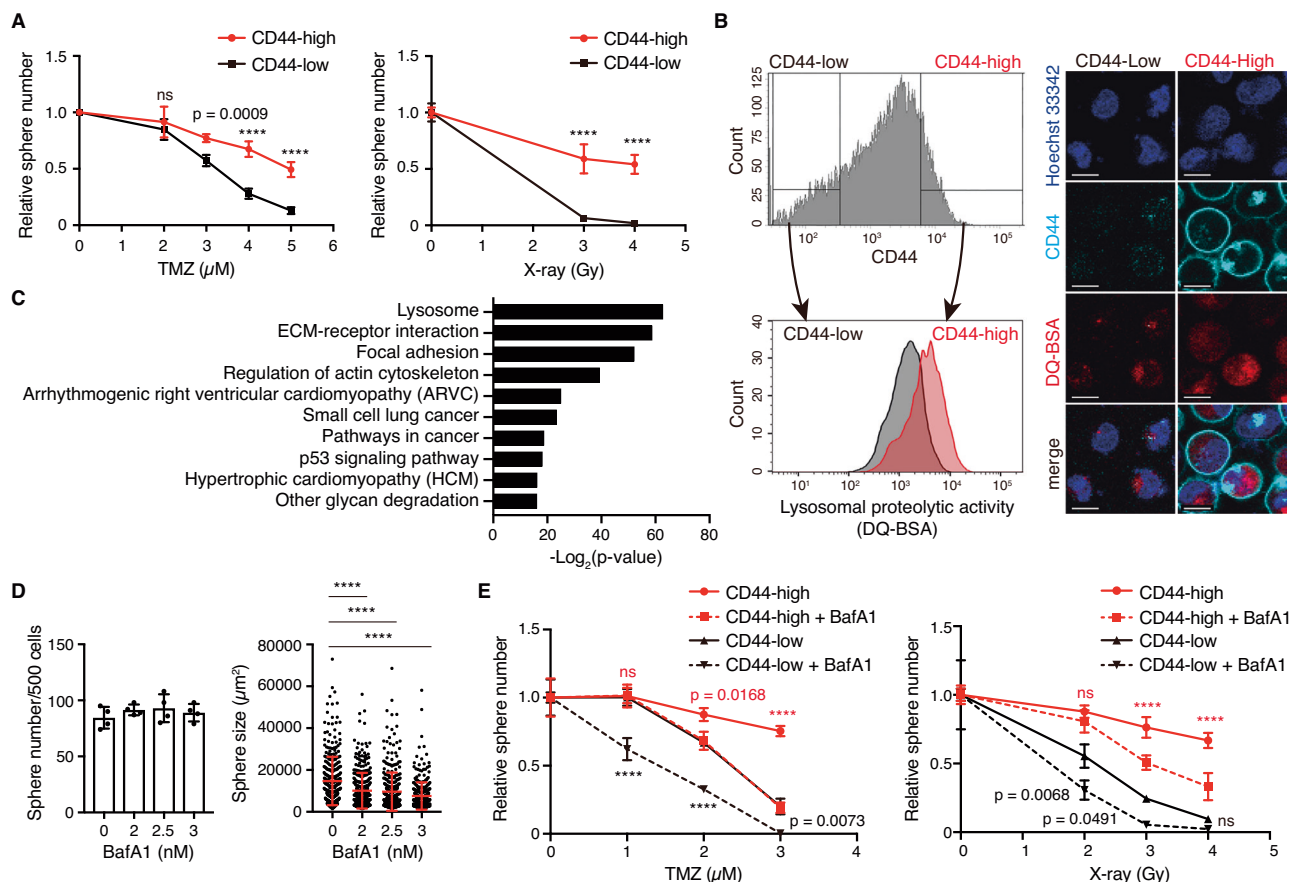

Fig. 2 | Lysosomal proteolytic activity contributes to therapeutic resistance in GBM. A TGS04 cells stained with fluorescently labeled anti-CD44 antibodies were sorted by a fluorescence-activated cell sorter into CD44-high (highest 15% of total) or CD44-low (lowest 15% of total) cells. Sensitivities of the CD44-high and CD44-low cells to TMZ and X-ray were examined by the sphere formation assay ($n = 3$ technical replicates). **B** After treatment with DQ-BSA for 6 h, the TGS04 cells were stained with fluorescently labeled anti-CD44 antibodies. The lysosomal proteolytic activity of CD44-high (highest 15% of total) or CD44-low (lowest 15% of total) cells was detected with flow cytometry and confocal fluorescence microscopy after separation on a fluorescence-activated cell sorter. Scale bars, 10 μm. **C** Gene ontology analysis (KEGG) for CD44-high and CD44-low TGS04 cells was

performed by using protein-coding genes with more than 2-fold difference (RPKM of CD44-high ≥ 10). **D** The sphere formation ability of TGS04 cells was examined in the presence or absence of 2-3 nM bafA1 ($n = 4$ technical replicates). **E** Sensitivities of CD44-high and CD44-low TGS04 cells to TMZ ($n = 3$) and X-ray ($n = 4$ technical replicates) were examined in the presence or absence of 2 nM (for TMZ) or 2.5 nM (for X-ray) bafA1. Data are presented as the means ± SD. Statistical significance (**A** and **E**) using a two-way ANOVA. Statistical analysis (**C**) using hypergeometric test. Statistical analysis (**D**) using unpaired two-tailed Student's t-tests. ns, not significant, ****$p < 0.0001$. Experiments were repeated at least three times with similar results. Source data are provided with this paper.

reported previously, CD44-high cells exhibited marked resistance to conventional GBM therapies, including TMZ and radiation (Fig. 2A). To investigate the linkage between lysosomal proteolytic activity and CD44 expression, we employed flow cytometry and confocal microscopy to measure lysosomal proteolytic activity. Results from the DQ-BSA assays revealed that CD44-high cells displayed higher levels of lysosomal proteolytic activity compared with CD44-low cells (Fig. 2B). RNA-sequencing analysis of CD44-high and CD44-low cells (TGS04)

also unveiled a significant activation of lysosome-related signatures in CD44-high cells (Fig. 2C). Importantly, the correlation between CD44 expression and lysosomal proteolytic activity held true across all the GBM cell lines examined (Supplementary Fig. 2A, B).

To further explore the impact of lysosomal proteolytic activity on the response to conventional anti-GBM treatment, we conducted experiments involving the administration of a lysosomal inhibitor, bafilomycin A1 (bafA1), in conjunction with TMZ or X-ray. The

application of bafA1 (2–3.5 nM) demonstrated no discernible effect on the sphere formation ability of GBM cells, yielding only a modest reduction in sphere size (Fig. 2D). Remarkably, however, bafA1 significantly heightened the sensitivity of GBM cells to TMZ or radiation therapy (Fig. 2E). This is consistent with previous report that application of an autophagy inhibitor enhanced the cytotoxicity of TMZ in malignant gliomas[25]. These results substantiate the critical role played by lysosomal proteolytic activity in influencing the responsiveness of GBM to cancer therapy.

TFE3 governs metabolic activity to augment the malignant signature

In our pursuit to unravel the mechanism governing lysosomal activity in GBM, we directed our attention toward the MiT/TFE family of transcription factors, which includes TFEB, TFE3, TFEC, and MITF. These transcription factors are known to be master regulators of lysosomal biogenesis and are influential in shaping cancer phenotypes. As a result, we postulated that a member of the MiT/TFE family might also play a role in promoting lysosomal activity and tumorigenicity in gliomas. The gene expression analysis revealed that among the MiT/ TFE family members, TFE3 exhibited the highest abundance in GBM cell lines, whereas the expression of TFEB, TFEC, and MITF was notably low (Supplementary Fig. 3A). Notably, the TFE3 protein in CD44-high (Lyso-high) cells was abundant with nuclear localization, while it was remarkably reduced in CD44-low (Lyso-low) cells (Fig. 3A). The expression level of TFE3 protein is much higher in Lyso-high GBM cell lines than the Lyso-low GBM cell lines (Supplementary Fig. 3B). To establish a causative relationship between TFE3 and lysosomal function, we generated GBM cells with *TFE3*-knockout (*TFE3*-KO) and *TFE3*-overexpression (*TFE3*-OE). The results from the DQ-BSA assays demonstrated that *TFE3*-KO led to a significant reduction in lysosomal proteolytic activity in GBM cells, while *TFE3*-OE had the opposite effect (Fig. 3B, Supplementary Fig. 3C, D). Furthermore, we used the Lyso-Tracker probe to show that *TFE3*-KO reduced the volume of the acidic compartment, including lysosomes (Supplementary Fig. 3E). A decrease in cathepsin B activity and an increase in lysosomal pH were also observed in *TFE3*-KO GBM cells (Supplementary Fig. 3F, G), indicating that *TFE3* loss induced lysosomal dysfunction in GBM cells. By contrast, *TFEB* loss did not affect lysosomal proteolytic or cathepsin B activity (Supplementary Fig. 3H, I). Additionally, we observed that the *TFE3*-OE inhibited LLOMe-induced LMP (Fig. 3C, Supplementary Fig. 3J). These findings collectively emphasize the essential role of TFE3, but not TFEB, in maintaining lysosomal function in GBM cells.

To explore the roles of TFE3 in the malignant properties of GBM cells, we conducted a functional analysis involving GBM cells with either *TFE3*-OE or -KO. We observed that the deficiency of *TFE3*, but not *TFEB*, in GBM cells, led to a reduction in both the number and size of spheres in vitro (Fig. 3D, Supplementary Fig. 3K). Conversely, the *TFE3*-OE in GBM cells with Lyso-high activity, such as TGS04, did not exhibit significant effects in the sphere-forming assay. However, it significantly increased the size of individual spheres derived from GBM cells with Lyso-low activity, like KGS22, KGS03, and KGS04 (Fig. 3E, Supplementary Fig. 3L). These observed biological phenotypes were in line with the results from GSEA of RNA-sequencing data, which indicated that *TFE3*-OE activated malignancy-related pathways (e.g., the expression of Myc targets) and metabolic pathways (e.g., oxidative phosphorylation and mTOR signaling) (Supplementary Fig. 3M). In contrast, the *TFE3*-KO led to the repression of these pathways (Supplementary Fig. 3N), underscoring the pro-tumorigenic role of TFE3 under certain metabolic conditions.

TFE3 controls metabolic alterations to induce TMZ tolerance

To investigate the contribution of TFE3-driven metabolic alterations to drug tolerance, we assessed the impact of *TFE3*-OE on the cell survival of GBM cells. The *TFE3*-OE consistently heightened tolerance to TMZ in

various GBM cell lines (Fig. 3F, Supplementary Fig. 3O). For the characterization of *TFE3*-OE cells, we monitored TFE3 protein levels through GFP fluorescence in GBM cells expressing the TFE3-GFP fusion gene. This approach was chosen as TFE3 activity is regulated by post-translational modification rather than mRNA expression. The majority of TFE3-high (GFP-high) cells belonged to the CD44-high cell population, while CD44-low cells exhibited low levels of TFE3 expression (Fig. 3G). As expected, TFE3-high cells displayed elevated lysosomal proteolytic activity (Fig. 3H). The lysosomal activation in TFE3-high (GFP-high) cells was associated with heightened mitochondrial activity (Fig. 3I). Interestingly, the TFE3-high; CD44-high cells were significantly enriched following TMZ treatment, indicating their status as TMZ-tolerant persister cells (Fig. 3J). Inhibition of lysosomal activity by bafA1 resulted in a notable decrease in mitochondrial membrane potential, mitochondrial ROS, and oxygen consumption rate (OCR), emphasizing the intimate link between lysosomal activity and mitochondrial activation in GBM (Fig. 3K–M). Thus, the TFE3-lysosome axis orchestrates metabolic alterations, leading to TMZ tolerance in GBM.

TFE3-mediated induction of PGC1α regulates characteristics of Lyso-high cells

To investigate the mechanism by which TFE3 regulates the phenotypes of Lyso-high GBM cells, we first compared the expression levels of direct TFE3 targets identified through a public database based on ChIP-sequence experiments (https://rnasysu.com/chipbase3/)[26,27], in *TFE3*-KO and *TFE3*-OE GBM cells relative to their respective controls (Fig. 4A). Additionally, we compared the expression of these TFE3 targets between Lyso-high and Lyso-low GBM cell lines (Fig. 4B). We found that six targets were commonly downregulated in Lyso-low and *TFE3*-KO GBM cells, whereas they were upregulated in Lyso-high and *TFE3*-OE GBM cells (Fig. 4B). Notably, among these six TFE3 targets, peroxisome proliferator-activated receptor-gamma coactivator 1-alpha (PGC1α), encoded by *PPARGC1A*, has been reported as a key regulator of mitochondrial biogenesis associated with tumor malignancy and poor prognosis[28]. Therefore, we explored whether PGC1α is involved in the TFE3-mediated phenotypes of Lyso-high GBM cells.

To investigate the role of PGC1α, we overexpressed PGC1α in GBM cells and assessed its effects. We found that PGC1α overexpression (PGC1α-OE) led to increased mitochondrial activity, as measured by JC-10 and MitoSOX (Fig. 4C, D). Additionally, PGC1α-OE enhanced lysosomal proteolytic activity, increased cathepsin B activity, and suppressed LLOMe-induced lysosomal membrane permeabilization (LMP) (Fig. 4E–G), indicating that PGC1α supports both lysosomal and mitochondrial functions. Whereas, in Lyso-high cells, *TFE3*-KO inhibited their proliferation significantly, PGC1α-OE counteracted the inhibitory effect of *TFE3*-KO (Fig. 4H), indicating that PGC1α is a critical target of TFE3. Notably, an increase of sphere size by PGC1α-OE was observed only in Lyso-low GBM cells (KGS22) but not in Lyso-high cells (TGS04); we presume because of the difference in endogenous PGC1α expression in these cells (Fig. 4H, I). Furthermore, we found that PGC1α-OE conferred some resistance to TMZ treatment in GBM cells (Fig. 4J), suggesting that PGC1α is one of the TFE3 targets regulating the phenotypes of Lyso-high GBM cells.

We also investigated how TFE3 expression is regulated in GBM cells. Because calcium signaling is a key regulator of lysosomal activity in GBM, as previously shown in Supplementary Fig. 1L–O, we focused on the involvement of calcium in the regulation of TFE3 in GBM. BAPTA treatment reduced TFE3 levels (Supplementary Fig. 4A), suggesting that intracellular calcium modulates lysosomal activity mediated by TFE3. To identify mediators in the calcium signaling pathway contributing to TFE3 activation, we tested various inhibitors and activators targeting calcium-related molecules, including calcineurin, CAMKK, AKT, mTORC1, and AMPK. Among these, only the AMPK inhibitor and activator consistently decreased and increased TFE3 levels, respectively (Supplementary Fig. 4B). Upregulation of TFE3 by the AMPK
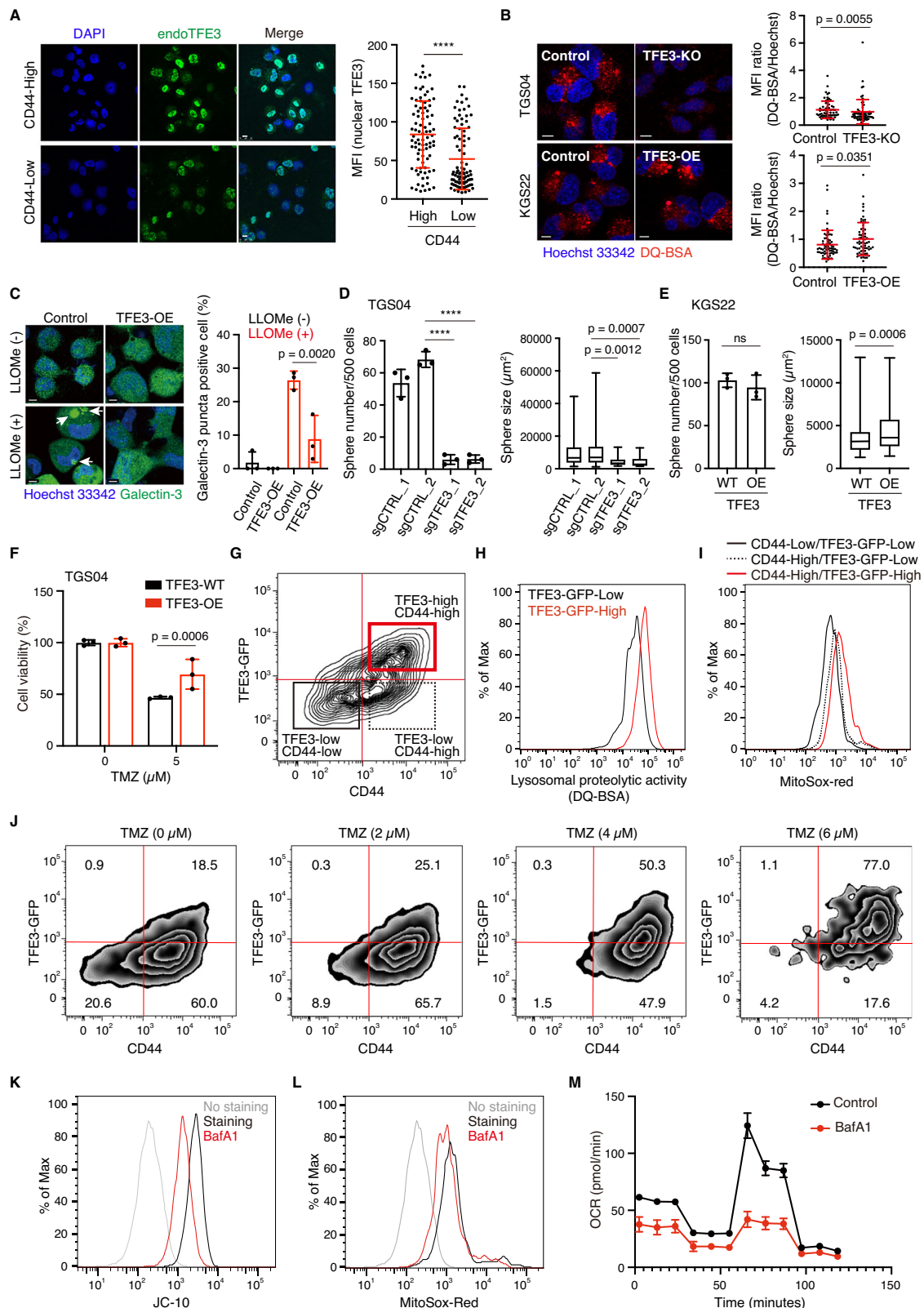
activator was abolished by BAPTA, indicating that calcium is essential for AMPK-induced upregulation of TFE3 (Supplementary Fig. 4C). Whereas, calcium concentrations, measured by using the Turquoise Calcium Fluorescence LIfeTime Sensor (Tq-Ca-FLITS)[29], were not necessarily correlated with lysosomal proteolytic activity in GBM cell lines (Supplementary Fig. 4D). We assume that more complex mechanisms underlie the regulation of TFE3 and lysosomal function in

GBM cells. Thus, although further analysis is warranted, we assume that calcium and AMPK pathways play critical roles in drug tolerance mediated by the TFE3–lysosomal axis in GBM.

TFE3 provides functional advantages in the malignancy of GBM

To investigate the clinical relevance of TFE3 in the malignant phenotypes of GBM cells, we initially evaluated the expression of TFE3 in

Fig. 3 | TFE3-lysosome pathway enhances the tolerance of GBM therapy. A The representative images of TFE3 protein levels in sorted CD44-high and CD44-low TGS04 cells by immunocytochemistry and quantification of mean fluorescence intensity of nuclear TFE3 (CD44-high $n = 87$; CD44-low $n = 89$). Scale bars, 10 μm. **B** The representative images and quantification of the fluorescence intensity of DQ-BSA associated with lysosomal proteolytic activity (Control $n = 67$, TFE3-KO $n = 64$; Control $n = 65$, TFE3-OE $n = 67$). Scale bars, 10 μm. **C** The representative images and quantification of galectin-3 punctation in *TFE3*-WT and *TFE3*-OE TGS04 cells after treatment with LLOMe (50 μM) for 15 min ($n = 3$ independent samples). Scale bars, 10 μm. **D, E** Number and size of spheres formed by *TFE3*-WT and *TFE3*-KO TGS04 cells (**D**), or *TFE3*-WT and *TFE3*-OE KGS22 cells (**E**) ($n = 3$ technical replicates). **F** The effect of *TFE3*-OE on the sensitivity of TGS04 to TMZ was examined by the cell viability assay ($n = 3$ technical replicates). **G** Flow cytometric analyses of TFE3 and CD44 levels in which TGS04 cells expressing TFE3-EGFP. **H** Detection of lysosomal proteolytic activity for TFE3-EGFP-low (lowest 15% of total) and TFE3-EGFP-high (highest 15% of total) TGS04 cells. **I** Evaluation of mitochondrial ROS in indicated subpopulations of TGS04 cells. **J** The ratio of the CD44-high/TFE3-EGFP-high TGS04 cells to total cells after treatment of TMZ for 5 days. **K–M** Mitochondrial membrane potential (**K**), mitochondrial ROS (**L**), and oxygen consumption rate (OCR) (**M**) were detected in TGS04 cells after treatment of 5 nM bafA1 for 16–24 h. ($n = 3$ independent samples, data are presented as the means ± SEM for OCR). Data are presented as the means ± SD. For the boxplots, (**D, E**), the line inside the box shows the median value. The bounds of the box represent the 25th–75th percentiles, with whiskers at minimum and maximum values. Statistical comparison (**A, B, E**) using unpaired two-tailed Student's t-tests. Statistical comparison (**C, D**) using a one-way ANOVA. Statistical comparison (**F**) using a two-way ANOVA. ns, not significant, ****$p < 0.0001$. Experiments were repeated at least three times with similar results. Source data are provided with this paper.

tumor tissue sections derived from glioma patients with intermediate-to high-grade gliomas via immunohistochemistry. We observed that the TFE3 protein was barely expressed in normal brain tissue, whereas it was highly expressed in brain tissue from glioma patients (Fig. 5A). Of note, we found that the TFE3 protein levels were positively correlated with the severity of malignancy. Specifically, GBM tumors were characterized by particularly high expression of nuclear TFE3 protein. The analysis of TFE3 protein expression clearly indicated that high TFE3 protein levels were a poor prognostic marker for the progression-free survival (PFS) of patients with glioma (Fig. 5B, C). This implies that TFE3 protein is a clinical indicator of malignant progression in GBM. By contrast, analysis of The Cancer Genome Atlas (TCGA) glioma dataset, which includes data from patients with Grade 2, 3, and 4 (GBM) gliomas, showed that higher expression of *TFE3* mRNA was significantly, but weakly, associated with shorter survival (Supplementary Fig. 5A, B). This suggests that the TFE3 protein level is mainly post-translationally, but not transcriptionally, regulated. To evaluate the function of TFE3 in vivo, GBM cells were orthotopically transplanted to the mice. The data showed that the survival of mice bearing *TFE3*-KO GBM cells was significantly extended compared with that of mice bearing control cells (Fig. 5D). Conversely, the survival of mice bearing *TFE3*-OE GBM cells was shorter than that of mice bearing the control cells (Fig. 5E). Taken together, the above data indicate that the activation of TFE3 plays a crucial role as a regulator of malignant properties in GBM.

Lysine is an essential amino acid to maintain lysosomal function in GBM

To gain insights into the specific metabolic regulation associated with lysosomal activity, we endeavored to identify differences between the Lyso-high and Lyso-low groups through transcriptional and metabolome analyses. Our gene ontology analysis of upregulated genes revealed that several metabolic pathways, such as amino acid transport, were augmented in the Lyso-high group compared with the Lyso-low group (Supplementary Fig. 1L). To assess the metabolic status of the two groups of GBM cells, we conducted a comprehensive and quantitative analysis utilizing capillary electrophoresis mass spectrometry (CE-MS). Metabolite set enrichment analysis (MSEA) of the quantified metabolites revealed significant enrichment in amino acid metabolism (Fig. 6A), such as the pathways of methionine metabolism, histidine metabolism, and glycine and serine metabolism. Since it is well-established that mTOR-mediated autophagy pathways are regulated by amino acids, such as branched-chain amino acids (BCAA), we focused on investigating the role of amino-acid-related signaling pathways in the response of GBM cells to cancer therapy. As the depletion of BCAAs activates the autophagy pathway[30], we explored whether these amino acids also influenced lysosomal proteolytic activity in GBM cells. To accomplish this, we incubated GBM cells with media lacking L-valine, L-leucine, or L-isoleucine for a specified period (Fig. 6B). Lysosomal proteolytic activity was then assessed using the

DQ-BSA assay. While bafA1 (the positive control) markedly inhibited lysosomal activity, the depletion of each BCAA had a weak effect. Unexpectedly, we discovered that the depletion of lysine significantly reduced lysosomal proteolytic activity (Fig. 6B, Supplementary Fig. 6A–D).

Lysine is an essential amino acid that plays a key role in various biological processes, including protein synthesis and calcium absorption[31]. While it has been reported that cancer cells have higher levels of lysine-degrading enzymes[32], the correlation between lysine metabolism and cancer malignancy, particularly resistance of GBM to therapy, was largely unknown. Although a recent study has provided insights into the impact of lysine restriction on its catabolic pathways, affecting antitumor immunity[23], and another study has found that lysine restriction inhibits the lysosome pathway and mitochondrial oxidative phosphorylation in adipocytes[33], the complex relationship between lysine and lysosomal function in GBM cells remains poorly understood. Consequently, we elucidated the potential of modulating the lysine pathway as a mechanism to induce lysosomal dysfunction in GBM cells. While lysine depletion alone did not impact lysosomal vulnerability, it did enhance LLOMe-induced LMP (Fig. 6C, Supplementary Fig. 6E), suggesting a crucial role for lysine in maintaining lysosomal membrane integrity. To investigate the specificity of the lysine effect, we determined the effect of other essential amino acids in a lysosomal galectin-3 punctation assay. GBM cells expressing mCherry-LAMP1 (a lysosomal membrane protein) and EGFP-Gal3 (at low levels to reduce pseudo puncta) were treated with LLOMe after incubation for 16–24 h in media lacking specific essential amino acids (Supplementary Fig. 6F). We observed that a low dose of LLOMe did not induce galectin-3 puncta in cells incubated in the control medium containing all amino acids. However, LLOMe treatment did induce galectin-3 punctation under methionine or lysine-depleted conditions, but not when other essential amino acids were depleted. Notably, only lysine depletion, but not methionine depletion, suppressed lysosomal proteolytic activity (Fig. 6B). Therefore, we focused on lysine depletion for further analysis. As anticipated, complete lysine depletion (standard media; lysine 500 μM) inhibited sphere formation significantly, as did other essential amino acid depletion (Supplementary Fig. 6G). Subsequently, we investigated the influence of restricted lysine on sphere formation. Cultivating GBM cells in 3% lysine (15 μM) moderately reduced sphere formation (Fig. 6D, E). Under this condition, we observed that lysine limitation heightened the sensitivity of the cells to LLOMe treatment (Fig. 6F). Thus, we have demonstrated that lysine is an indispensable amino acid central to preserving lysosomal robustness, thereby shielding GBM cells from lysosomal damage.

Lysine maintains lysosomal function by antagonizing NO production

Lysine serves as an anti-metabolite of arginine in various biological contexts[34]. Lysine inhibits cellular arginine transport through system y+, a high-affinity, Na+-independent transporter for arginine, lysine, and

ornithine[35,36]. Additionally, lysine acts as a selective modulator of iNOS activity to suppress NO overproduction[37]. To gain a mechanistic understanding of how lysine regulates lysosomal function, we first evaluated the effect of arginine on lysosomal proteolytic activity by

increasing the arginine to lysine ratio (25 mM and 0.5 mM, respectively) in the culture media. The DQ-BSA assay confirmed that excess arginine led to the suppression of lysosomal proteolytic activity (Fig. 7A). In line with the induction of lysosomal vulnerability due to lysine depletion,
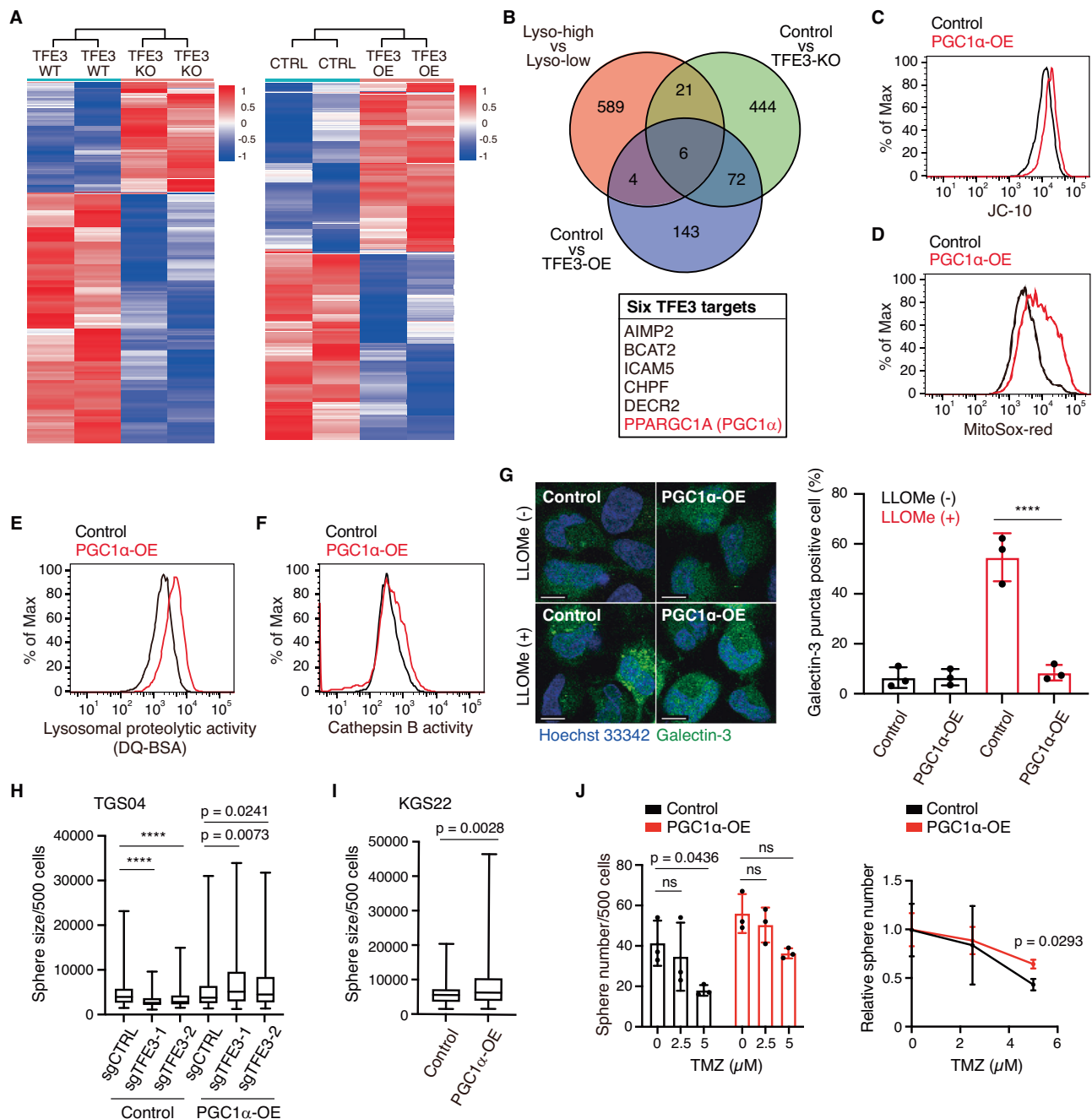
Fig. 4 | TFE3-induced Lyso-high GBM phenotypes are mediated by PGC1α. A The expression level of *TFE3* targets was compared between *TFE3*-WT and *TFE3*-KO TGS04 cells or *TFE3*-OE and control KGS22 cells. **B** A Venn diagram and table showing the common *TFE3* targets among the 3 indicated groups. **C, D** Mitochondrial membrane potential (**C**), mitochondrial ROS (**D**) of PGC1α-OE TGS04 cells were detected with JC-10, MitoSOX, respectively. **E, F** lysosomal proteolytic activity and cathepsin B activity of PGC1α-OE TGS04 cells were measured by flow cytometry. **G** The representative images and quantification of galectin-3 punctation in control and PGC1α-OE TGS04 cells after treatment with LLOMe (50 μM) for 15 min (*n* = 3 independent samples). Scale bars, 10 μm. **H** The sphere size formed in a medium containing 1% methylcellulose by control and *TFE3*-KO (sgTFE3-1 and sgTFE3-2) TGS04 cells with or without PGC1α-OE was evaluated (Control: sgCTRL *n* = 134; sgTFE3-1 *n* = 100; sgTFE3-2 *n* = 113; PGC1α-OE: sgCTRL

n = 152; sgTFE3-1 *n* = 85; sgTFE3-2 *n* = 128). **I** The sphere-forming ability of KGS22 cells was evaluated in a medium containing 1% methylcellulose by sphere size in indicated conditions (*n* = 3 technical replicates). **J** The sensitivity of control and PGC1α-OE TGS04 cells to TMZ was examined by sphere formation assay after 10 days of treatment (*n* = 3 technical replicates). For the boxplots (**H, I**), the line inside the box shows the median value. The bounds of the box represent the 25th–75th percentiles, with whiskers at minimum and maximum values. Data are presented as the means ± SD. Statistical comparison (**G, H**) using a one-way ANOVA. Statistical comparison (**I**) using two-tailed Student's *t*-tests. Statistical comparison (**J**) using a two-way ANOVA. ns, not significant. Experiments (**H–J**) were repeated at least two times with similar results, other experiments were repeated at least three times with similar results. Source data are provided with this paper.
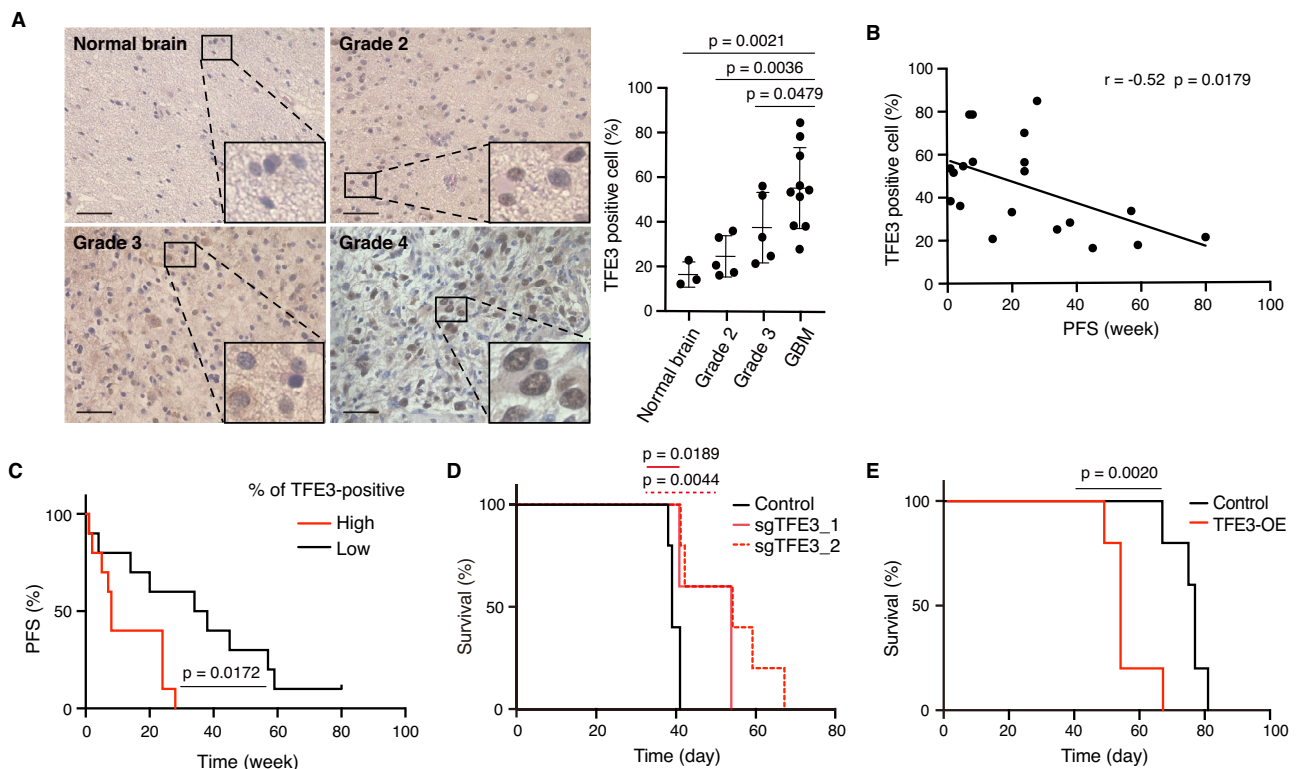
Fig. 5 | TFE3 contributes to the malignant progression of GBM. A Representative images of tissue sections immunostained with TFE3 antibody and quantification of TFE3-positive cells. Normal tissue ($n = 3$ biological replicates), Grade 2 ($n = 5$ biological replicates), Grade 3 ($n = 5$ biological replicates), and Grade 4 ($n = 10$ biological replicates) sections from independent patients. Scale bars, 50 μm. **B** Correlation analysis of the progression-free survival of glioma patients and their percentage of TFE3-positive cells from (**A**). **C** Kaplan–Meier survival curves of glioma patients bearing higher (red) or lower (black) percentages of TFE3-positive cells (relative to the average percentage of TFE3-positive cells) from (**A**). **D**, **E** Kaplan–Meier survival curves of nude mice transplanted with the *TFE3*-WT (black) and *TFE3*-KO (red) TGS04 cells (**D**), or control (black) and *TFE3*-OE (red) KGS22 cells (**E**). $n = 5$ mice per group. Data are presented as the means ± SD. Statistical comparison (**A**) using a one-way ANOVA. Statistical comparison (**B**) using Pearson correlation analysis. Statistical comparison (**C**–**E**) using Kaplan–Meier method with the log-rank test. Source data are provided with this paper.

excess arginine increased LLOMe-induced LMP, reduced the number of spheres, and sensitized GBM cells to LLOMe in a sphere formation assay (Fig. 7B, C, Supplementary Fig. 7A). These findings suggested that the lysine-arginine balance regulated lysosomal membrane integrity.

Given that arginine can follow various metabolic pathways, including acting as a precursor for nitric oxide (NO), creatine, and agmatine[38], we explored the potential metabolic contribution of arginine-metabolizing enzymes, including NO synthase, arginase, arginine decarboxylase, and arginine-glycine amidinotransferase (Supplementary Fig. 7B). Based on the data of RNA-sequencing, the gene expression of arginine decarboxylase (*ADC*) and arginine-glycine amidinotransferase (*GATM*) was extremely low in GBM cells (Supplementary Fig. 7C). Furthermore, the arginase inhibitor (Nor-NOHA) did not influence the regulation of lysosomal proteolytic activity and the sensitivity of GBM cells to TMZ treatment (Fig. 7D, E), indicating that arginase is not involved in this phenomenon. Considering that arginine is a substrate for NO synthase (NOS) and the primary precursor of NO[39], we assessed NO production in GBM cells using diamino fluorescein-FM diacetate (DAF-FM DA). Our observations revealed that an excess of arginine (25 mM), along with lysine depletion, increased NO levels (Fig. 7F). Given that the accumulation of NO has been associated with LMP[40], we examined whether the NO level affected lysosomal function. Treatment with an NO inducer (NOC-18), as well as an excess of arginine, resulted in a suppression of lysosomal proteolytic activity (Fig. 7G). Importantly, L-NAME, an inhibitor of NOS, reversed the lysosomal dysfunction induced by lysine depletion (Fig. 7H, I). These data collectively demonstrate that lysine depletion leads to

lysosomal dysfunction by increasing NO production, which is attributed to the greater availability of arginine (Fig. 7J).

Lysine restriction and its mimetic boost therapeutic efficacy in GBM

Recent advances in cancer metabolism research have revealed that nutritional interventions are effective at controlling tumor growth[41]. Therefore, appropriate combinations of specific cancer therapies with altered nutrition could considerably improve the efficacy of either therapy alone[42,43]. Because bafA1 increased the antitumor effects of TMZ, we investigated whether lysine restriction enhances the efficacy of practical anticancer therapy used in clinics, including TMZ. We found that restricting only lysine (2%–3% lysine in the culture medium), but not other essential amino acids, enhanced the sensitivity of GBM cells to TMZ in a spheroid formation assay (Fig. 8A, Supplementary Fig. 8A–H).

While we have indeed found a possible application of lysine restriction in GBM treatment, it is important to acknowledge that the feasibility of implementing a lysine restriction diet in practical therapy may be limited by potential toxicity concerns. Therefore, our focus shifted toward identifying alternative approaches to harness lysine restriction's effects to circumvent this potential hurdle. As a result, we investigated the use of homoarginine, a natural arginine homolog, for inducing lysosomal dysfunction. Homoarginine can be the substrate for several NOS isoforms, which produce NO in addition to arginine[44] (Fig. 8B). As consistent with previous reports, we showed that homoarginine markedly increased intracellular NO levels (Fig. 8C), suppressing lysosomal proteolytic activity and increasing the lysosomal pH (Fig. 8D, E, Supplementary Fig. 8I). Supplementation with homoarginine also
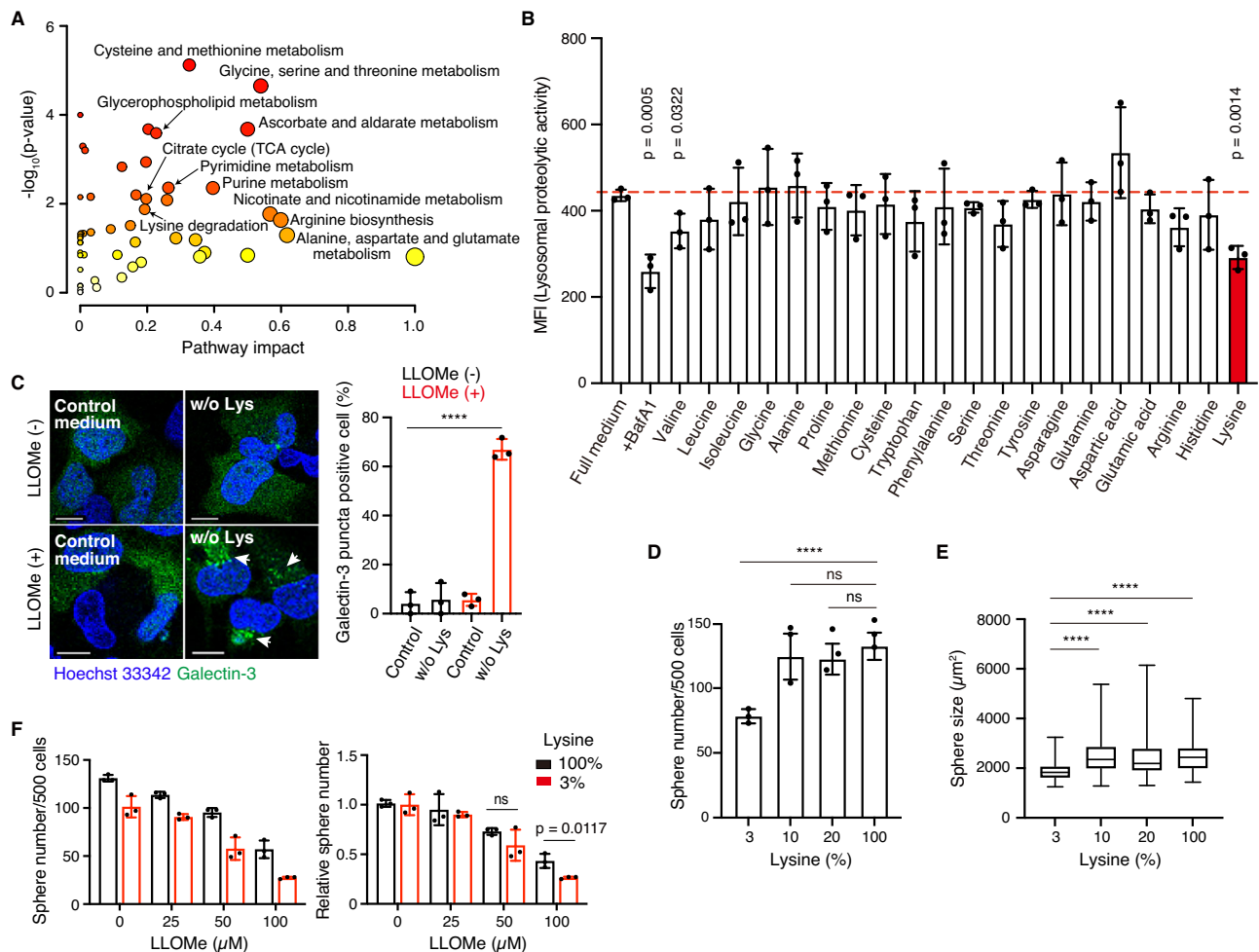
Fig. 6 | Lysine plays a vital role in protecting GBM cells against lysosomal damage. A Results of the metabolomic analysis, showing key nodes in metabolic pathways that have been significantly altered between Lyso-high and Lyso-low groups. The x-axis represents pathway impact, which was computed using topology analysis. **B** Quantification of lysosomal proteolytic activity measured with DQ-BSA fluorescence in TGS04 cells with flow cytometry after culture in single-amino-acid-depleted NSPC medium for 16–24 h ($n = 3$ independent experiments). **C** TGS04 cells expressing EGFP-Gal3 were pretreated in a complete culture medium (control medium) or lysine-depleted medium (w/o Lys) for 16–24 h. Galectin-3 punctation was then observed after 15 min of 50 μM LLOMe treatment. Percent of galectin-3 puncta-positive cells was quantified ($n = 3$ independent samples). Scale bars, 10 μm. **D, E** The sphere number (**D**) and size (**E**) formed by TGS04 cells were evaluated under lysine-restricted conditions by the sphere formation assay ($n = 3$). **F** The sensitivity of TGS04 cells to LLOMe was examined under lysine-restricted and normal conditions by the sphere formation assay ($n = 3$). For the boxplots (**E**), the line inside the box shows the median value. The bounds of the box represent the 25th–75th percentiles, with whiskers at minimum and maximum values. Data are presented as the means ± SD. Statistic comparison (**A**) using a weighted Z-test. Statistic comparison (**B**–**E**) using a one-way ANOVA. Statistic comparison (**F**) using a two-way ANOVA. ns, not significant, ****$p < 0.0001$. Experiments (**D**–**F**) were repeated at least three times with similar results. Source data are provided with this paper.

enhanced the TMZ sensitivity (Fig. 8F), while NOS inhibition with L-NAME partially reversed the increased sensitivity to TMZ induced by homoarginine (Supplementary Fig. 8J). By contrast, a substantial (25–50-fold) increase in the concentration of most essential amino acids did not significantly affect the sphere-forming ability or TMZ sensitivity (Supplementary Fig. 8K–S). The treatment by homoarginine enhanced the TMZ-induced apoptosis in the GBM cells (Supplementary Fig. 8T). The sensitivity enhanced by homoarginine was mediated through DNA damage because the overexpression of MGMT in TGS04 cells reversed their TMZ sensitivity (Fig. 8G). However, a GBM cell line, KGS23, which naturally expresses *MGMT*, showed a synergistic effect of homoarginine at high doses of TMZ (Fig. 8H), indicating that lysosomal dysfunction induced by homoarginine is effective in such *MGMT*-expressing TMZ-resistant cells. Notably, we did not observe a significant effect of combining homoarginine and TMZ on nontransformed human neural progenitor cells (Fig. 8I, Supplementary Fig. 8U, V).

Furthermore, in our pursuit of discovering additional anticancer drugs that exhibit a synergy effect with homoarginine, we conducted

a drug screening using a clinically available anticancer drug library consisting of 174 compounds. The results revealed that homoarginine enhanced the efficacy of numerous anticancer drugs including TMZ (Fig. 8J, Supplementary Data. 1). The selected drugs have been considered as potential candidates for a therapeutic approach to GBM (Fig. 8K, L, Supplementary Fig. 9A–C). Furthermore, similar to bafA1, homoarginine increased the sensitivity of GBM cells to X-ray (Fig. 8M). These findings suggest that lysosomal-targeting therapy may have broad applicability in enhancing the efficacy of GBM treatments.

Administration of homoarginine enhances the TMZ efficacy in vivo
Finally, to assess the impact of homoarginine on the therapeutic efficacy of TMZ in vivo, we orthotopically transplanted GBM cells labeled with luciferase into immunocompromised mice and subsequently evaluated the effects on tumor burden and survival. In this experiment, the mice were treated with homoarginine (200 mg/kg/day, i.p) for two
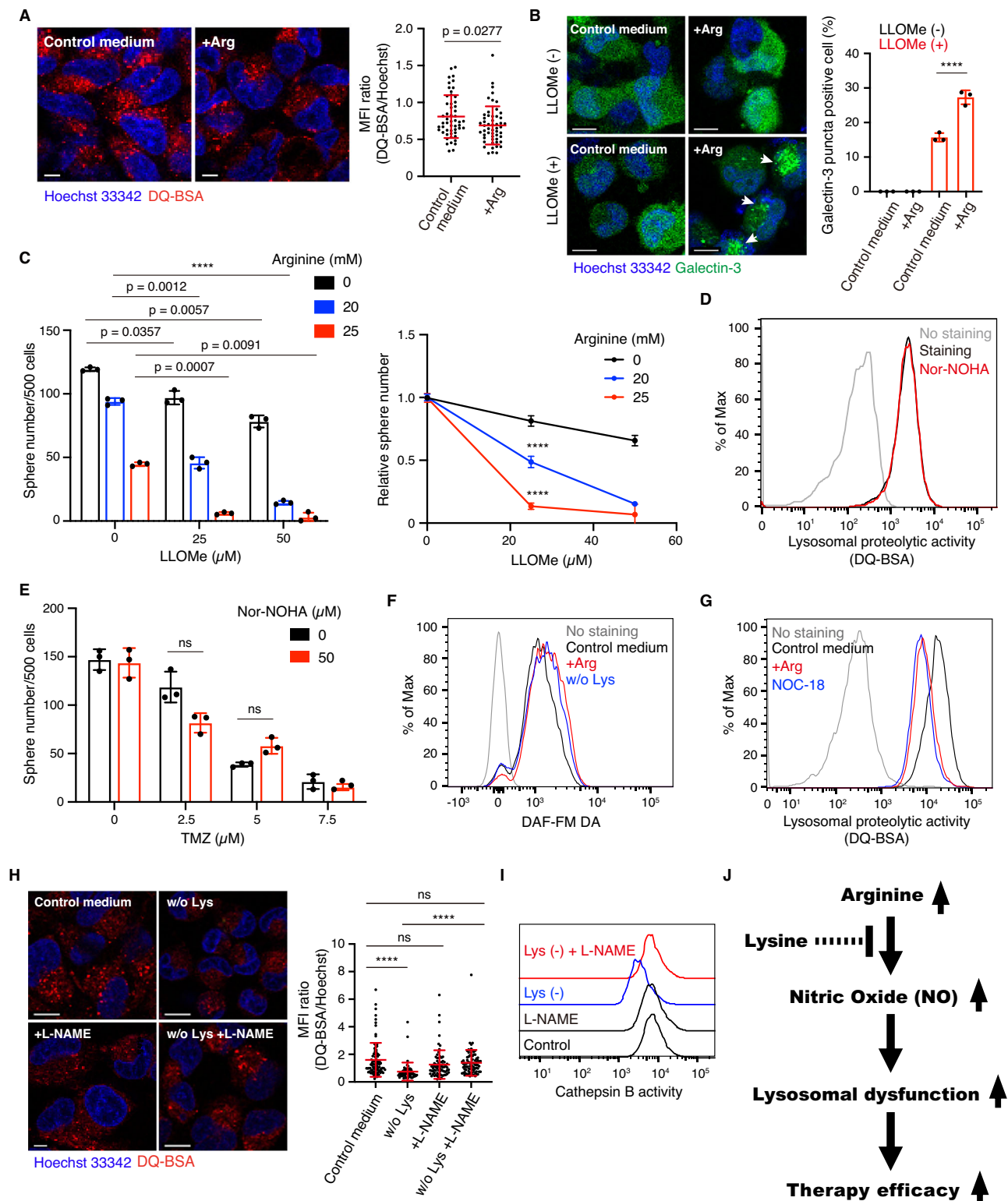
weeks after tumor cell inoculation, and/or TMZ (1.5 mg/kg/day, i.p.) for one week, as illustrated in (Fig. 9A). At 4 weeks after tumor cell inoculation, homoarginine alone did not significantly affect tumor growth, while both TMZ and TMZ/homoarginine combination remarkably suppressed tumor growth. However, at 6 weeks, although most of the mice treated with TMZ alone exhibited a remarkable tumor burden, those receiving TMZ/homoarginine combination still experienced significant suppression of GBM cells (Fig. 9B). Reduced lysosomal proteolytic and cathepsin B activity were observed in tumor cells from homoarginine-treated mice compared with their activity in

tumor cells from control mice (Supplementary Fig. 10A, B), indicating that homoarginine impaired lysosomal function in GBM cells in vivo. Consistently, the combined TMZ/homoarginine treatment significantly extended the survival of mice bearing GBM cells compared with TMZ alone (Fig. 9C), highlighting the enhancing effect of homoarginine on TMZ efficacy. This beneficial effect of homoarginine was also evident in a xenograft experiment involving different GBM cells (Fig. 9D, E). These data collectively demonstrate that the supplementation of homoarginine could be a potent therapeutic strategy to enhance the therapeutic effectiveness in GBM patients.

Fig. 7 | Lysine maintains lysosomal function by antagonizing the effect of arginine on NO synthesis. A Lysosomal proteolytic activity was imaged and quantified in TGS04 cells after pretreatment with 25 mM arginine (Arg) for 16–24 h ($n = 53$ cells/group). Scale bars, 10 µm. **B** The representative images and quantification of galectin-3 punctation after treatment of cells with 50 µM LLOMe for 15 min ($n = 3$ independent samples). TGS04 cells expressing EGFP-Gal3 were pretreated with 25 mM arginine (Arg) for 16–24 h. Scale bars, 10 µm. **C** Number and relative number of spheres formed by TGS04 cells in the presence of different concentrations of LLOMe with or without arginine (Arg) ($n = 3$ technical replicates). **D** Detection of lysosomal proteolytic activity in the TGS04 cells treated with 50 µM Nor-NOHA for 16–24 h. **E** Sensitivity of TGS04 to TMZ with or without Nor-NOHA ($n = 3$ technical replicates). **F** The level of nitric oxide (NO) was detected in the TGS04 cells after treatment with 25 mM arginine (Arg) or lysine-depleted medium (w/o Lys) with flow cytometry. **G** Detection of lysosomal proteolytic activity in the TGS04 cells treated with 25 mM arginine (Arg) or 200 µM NOC-18 with flow cytometry. **H** Representative images and quantification of lysosomal proteolytic activity in the TGS04 cells pretreated with 4 mM L-NAME for 3 h before exposure to lysine-depleted medium (w/o Lys) for 16–24 h (Control medium $n = 91$; w/o Lys $n = 58$; L-NAME $n = 72$; Lys+L-NAME $n = 83$). Scale bars, 10 µm. **I** Cathepsin B activity was measured in the TGS04 cells after pretreatment with 4 mM L-NAME for 3 h, followed by exposure to a lysine-depleted medium for 16–24 h. **J** Illustration showing the mechanism, by which lysine-arginine imbalance induces nitric oxide production, leading to lysosomal dysfunction. Data are presented as the means ± SD. Statistic comparison (**A**) using unpaired two-tailed Student's t-tests. Statistic comparison (**B** and **H**) using a one-way ANOVA. Statistic comparison (**C** and **E**) using a two-way ANOVA. ns, not significant, ****$p < 0.0001$. Experiments were repeated at least three times with similar results. Source data are provided with this paper.

Discussion

In this study, our discovery underscores the critical role of the TFE3-lysosome axis in the malignant properties of GBM (Fig. 9F). Moreover, we propose a unique strategy for impairing lysosomal function by modulating the lysine-arginine balance to improve the therapeutic efficacy of existing anti-GBM drugs (Fig. 9G). We refer to this approach as "Chemo-Boost Metabolite". Combining this metabolite with conventional therapy holds great promise in cancer treatment and may have real practical value.

The role of lysine in regulating malignant properties, such as chemoresistance, in cancer cells remains unclear. In this study, we demonstrated that NO production, controlled by the lysine-arginine balance, was crucial for maintaining lysosomal proteolytic activity and membrane integrity (Figs. 7J, 9G). While the precise mechanism by which NO regulates lysosomal membrane integrity is unclear, we proposed that NO-induced lysosomal membrane vulnerability via pro-oxidant events. This finding is consistent with previous reports showing that NO inhibits autophagy[45]. In our screening for TFE3 targets, we identified PGC1α—a key regulator of mitochondrial function—and found that PGC1α restored the *TFE3*-KO phenotype in sphere size. Additionally, a previous study indicated that PGC1α promotes lysosomal activity in a TFE3-dependent manner[46]. These findings suggest that PGC1α and TFE3 may form a collaborative network that enhances both lysosomal and mitochondrial functions. We propose that this close organelle communication may contribute to therapy resistance (Fig. 9F). As we previously reported, lysosomal membrane integrity is maintained by lysophagy, selective autophagy for damaged lysosomes[47]. We showed that the loss of lysophagy contributed to the sensitization of GBM cells to lysosomotropic compounds that induced LMP, resulting in an increase of intracellular Ca^{2+} levels and mitochondrial ROS-mediated cytotoxicity in GBM cells[47]. Therefore, lysine restriction therapy for inducing lysosomal vulnerability may be feasible in combination with a variety of anticancer drugs. Furthermore, lysosomal acidity facilitates the luminal accumulation of cytostatic weak bases and leads to their protonation, reducing their ability to pass the lysosomal membrane and causing lysosomal drug sequestration, known as the "safe house" effect[9,48,49]. A recent study showed that the efflux of TMZ to the outside of the cell via extracellular vesicles was suppressed by a lysosomal inhibitor[50]; the suppression of lysosomal efflux function may constitute a further reason for the therapeutic effect of lysine-arginine imbalance. On the other hand, we observed that lysosomal dysfunction induced by bafA1 or homoarginine increased radiation sensitivity, suggesting that the effect of lysosomal function on therapy resistance may not be solely dependent on drug sequestration and efflux. Unfortunately, we were unable to determine the precise mechanisms by which lysosomal dysfunction enhances TMZ efficacy due to the technical limitations of the present study. For instance, accurately measuring change in the intracellular distribution of TMZ remains challenging. Moreover, analyzing the effects of lysosomes on drug efficacy independently of mitochondria is problematic because these organelles are closely interconnected. Further research is warranted to understand better the role of lysosomes in therapeutic resistance in GBM cells.

In this study, we presented TFE3 as a regulator of GBM malignancy. Although TFEB and TFE3 appear to be crucial for the maintenance of neural stem cells via their involvement in lysosomal biogenesis[51], our data clearly demonstrated that TFE3, but not TFEB, plays a critical role in lysosomal biogenesis in GBM. TFE3 and TFEB share a common 10-base E-box-like palindromic sequence (GTCACGTGAC), called the Coordinated Lysosomal Expression and Regulation (CLEAR) element, which is typically located within 200 base pairs of the transcription initiation site and promotes autophagy and lysosomal biogenesis[52]. A crucial mechanism for the activation of TFEB and TFE3 involves the phosphorylation of their serine residues, which affects the cellular localization and nuclear export of these proteins[53]. Kinases such as mTORC1, protein kinase C, and AKT have been demonstrated to phosphorylate MiT/TFE family members, thereby influencing their localization and activity[54]. However, our findings demonstrated that GBM cells with TFE3 activation exhibited significant malignant phenotypes with mTORC1 activation. Therefore, an mTORC1-independent mechanism of TFE3 stabilization and nuclear localization mediated by calcium and AMPK may have contributed to GBM malignancy (Fig. 9F).

In summary, disrupting lysosomal function may provide a promising avenue for GBM therapy. A deeper understanding of the molecular mechanisms underlying the effects of lysine-arginine balance disruption may lead to the development of novel therapeutic strategies to improve the treatment of GBM and other cancers.

Methods
Study approval
Our research complies with all relevant ethical regulations. Patient-derived glioblastoma cell lines were obtained from Kanazawa University Hospital and Tokyo University Hospital. Informed consent was obtained from all participants. The study was approved by the Ethics Committee of Kanazawa University. Animal handling was carried out according to the protocols approved by the Committee on Animal Experimentation of Kanazawa University and performed following the university's guidelines for the care and use of laboratory animals (AP-204142). Regarding euthanasia: In the intracranial xenograft mouse model, mice were euthanized before death upon approaching the endpoint, defined by our IACUC protocol as a 20% loss of body weight with debilitations (e.g., severe hunching, lack of response to stimulation, or trembling). This limit was not exceeded in any of the experiments. Efforts were made, as much as possible, to alleviate pain and suffering.

Cell lines and culture
The human, patient-derived glioblastoma (GBM) cell line (TGS04) was established as described previously[55]. The seven additional human,
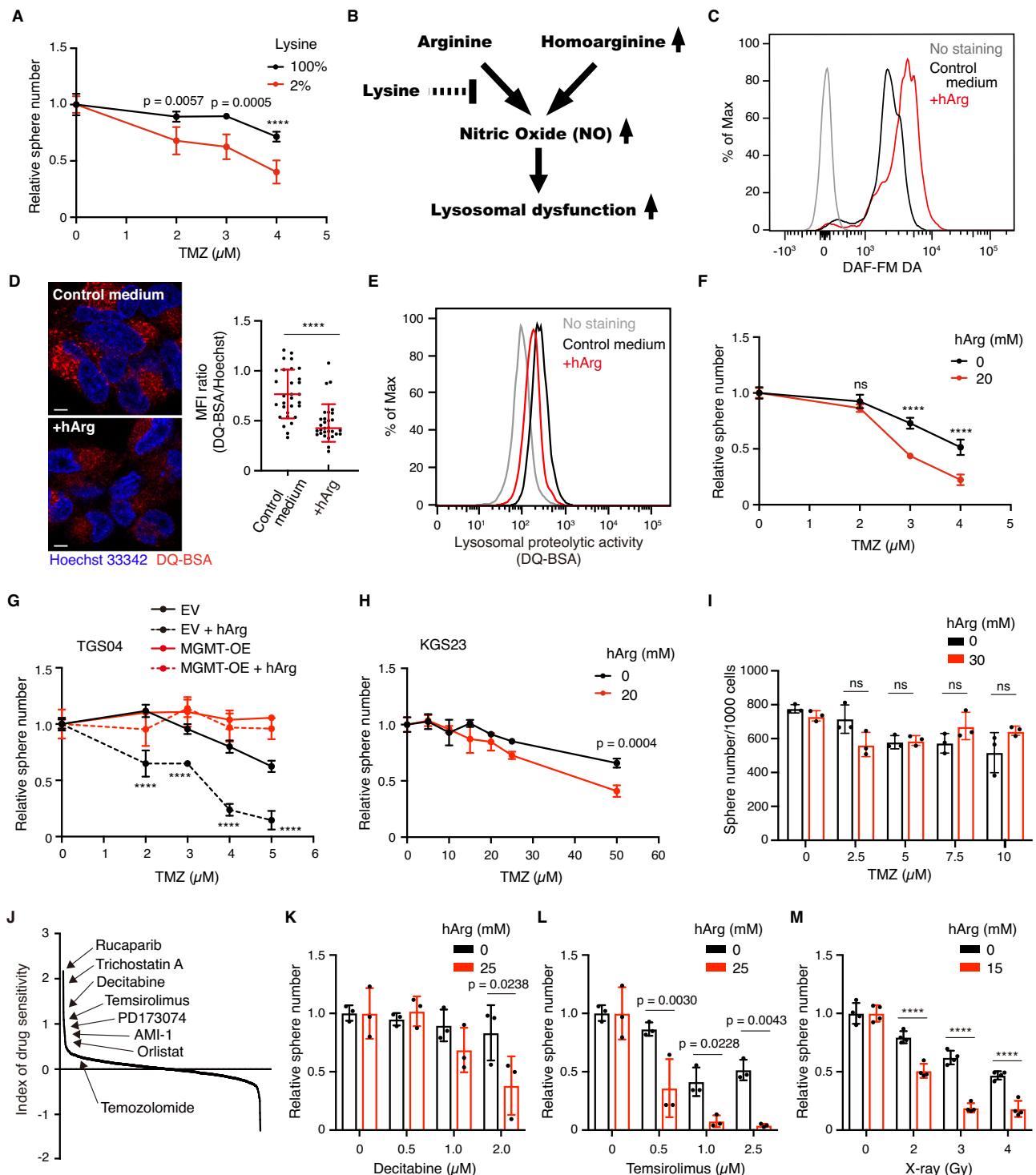
Fig. 8 | Lysine restriction and its mimetic boost the therapeutic efficacy.
A Sensitivity of TGS04 cells cultured in a lysine-restricted medium to TMZ was measured by the sphere formation assay ($n = 4$ technical replicates). **B** Illustration for the mechanism of homoarginine action on lysosomal function, in which homoarginine induces nitric oxide as a substrate of nitric oxide synthase. **C** Nitric oxide level in TGS04 cells was detected with DAF-FM DA after treatment with 30 mM homoarginine (hArg) for 16–24 h with flow cytometry. **D, E** Lysosomal proteolytic activity was detected after treatment with homoarginine (25 mM) for 16–24 h in TGS04 cells with confocal fluorescence microscopy (**D**) ($n = 30$ cells/group) and with flow cytometry (**E**). **F** Sensitivity of TGS04 to TMZ in combination of hArg ($n = 4$ technical replicates). **G** Sensitivity of TGS04 cells overexpressing *MGMT* to TMZ with or without homoarginine was measured ($n = 3$ technical replicates). **H** Sensitivity of KGS23 cells, which naturally express *MGMT*, to TMZ with or without homoarginine was measured ($n = 3$ technical replicates). **I** Quantification of

the number of spheres formed by neural progenitor cells treated with TMZ and hArg ($n = 3$ technical replicates). **J** Screening for drugs synergized with homoarginine to suppress GBM cell viability using a clinically available anticancer drug library consisting of 174 compounds. TGS04 cells were treated with 3 doses of anticancer drugs and 25 mM homoarginine for 2 days before cell viability assay. **K, L** Sensitivity of TGS04 cells to the indicated drugs in the presence or absence of homoarginine (hArg) ($n = 3$ technical replicates). **M** Sensitivity of TGS04 cells to X-ray in the presence or absence of hArg ($n = 4$ technical replicates). Data are presented as the means ± SD. Statistic comparison (**A, F–I, K–M**) using a two-way ANOVA. Statistic comparison (**D**) using unpaired two-tailed Student's *t*-tests. ns, not significant, ****p < 0.0001. Experiments (**I, K–M**) were repeated at least two times with similar results, other experiments were repeated at least three times with similar results. Source data are provided with this paper.
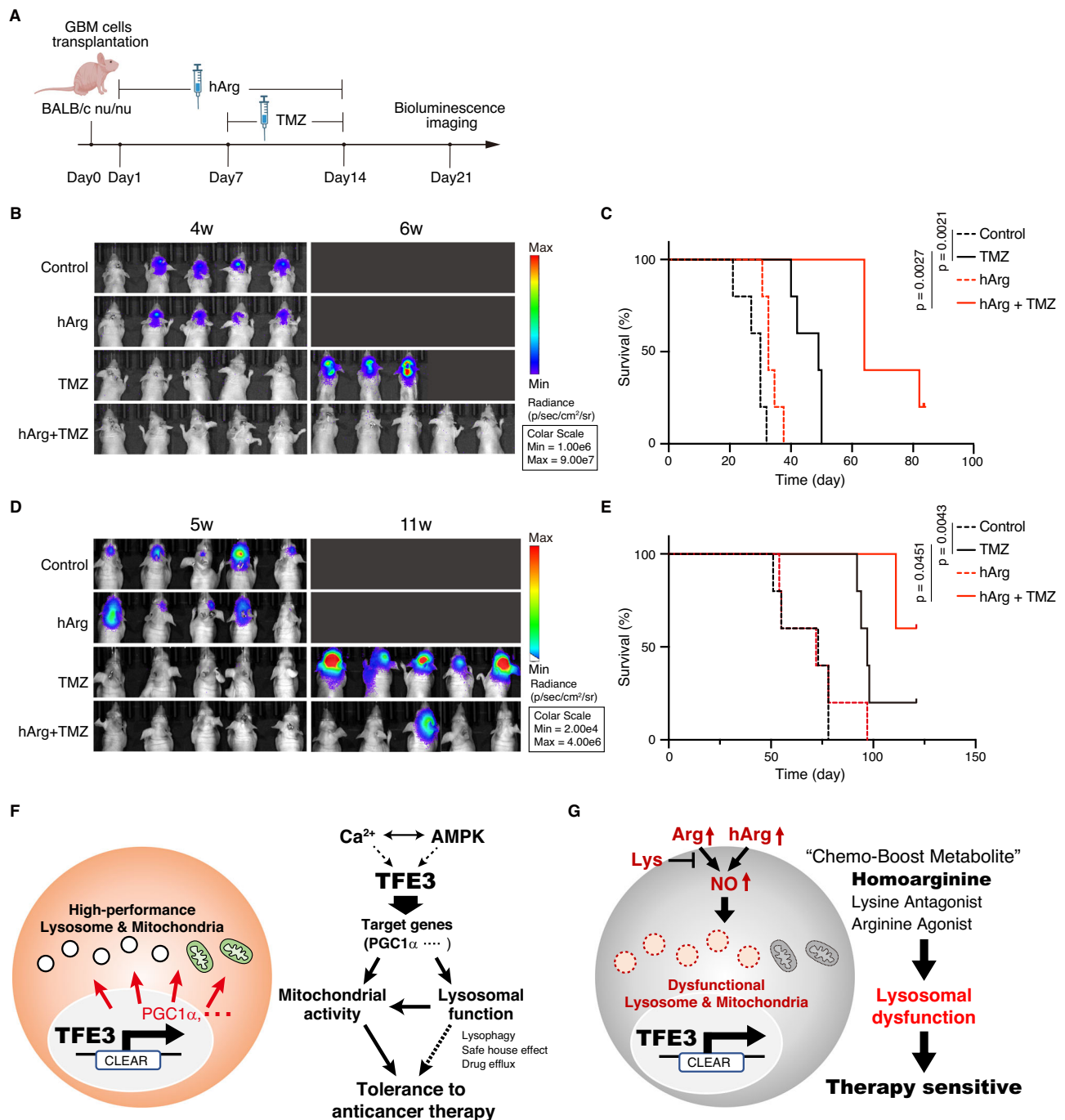
Fig. 9 | Combinational therapy of TMZ and homoarginine is a promising strategy for GBM therapy. A The treatment program by the intraperitoneal injection after intracranial transplantation with GBM cells. Created in BioRender. Yw (2024) https://BioRender.com/j77u897. **B–E** Luminescence imaging (**B, D**) and Kaplan–Meier survival analysis (**C, E**) of mice transplanted with TGS04 cells (**B, C**) or KGS10 cells (**D, E**) orthotopically (*n* = 5 mice/group). Mice were treated with DMSO control, TMZ (i.p. 1.5 mg/kg/mouse), hArg (i.p. 200 mg/kg/mouse), or hArg +TMZ. **F, G** The diagram shows the critical role of the TFE3-lysosome axis in the malignant properties of GBM (**F**). Imbalance of lysine-arginine by homoarginine improves the therapeutic efficacy through NO-mediated lysosomal dysfunction (**G**). Statistic comparison (**C, E**) using the Kaplan–Meier method with the log-rank test.

patient-derived glioma cell lines (KGS01, KGS03, KGS04, KGS07, KGS10, KGS15, KGS22, and KGS23) were established at the Department of Neuron Surgery, Kanazawa University, Japan from surgical specimens of primary GBM collected from 30 consenting patients (ages 30 to 90 years, of both genders) between 2015 and 2019[56–58]. In brief, each GBM surgical specimen was cut up and dissociated with accutase (STEMCELL Technologies, Vancouver, BC, Canada). The cells were cultured as spheroids, and passaging was repeated to establish a stem cell line. The established lines were used within 6 months after thawing

the stocks in this study. The use of human materials and protocols was approved by the Ethics Committees of Kanazawa University and the University of Tokyo. Human, patient-derived GBM spheroids were cultured on an ultra-low attachment culture plate (Corning, Corning, NY, USA) in neural stem progenitor cell (NSPC) medium, which contained DMEM/F12 (Gibco, Thermo Fisher Scientific, Waltham, MA, USA), B27 (Gibco), 5% penicillin/streptomycin (Thermo Fisher Scientific), hEGF (20 ng/mL, Sigma-Aldrich, St. Louis, MO, USA), and hFGF (20 ng/mL, Fujifilm Wako Chemicals, Osaka, Japan) at 37 °C in a

humidified atmosphere of 5% CO_2 and 5% oxygen. Custom media were used for the amino acid depletion experiments (DMEM/F12 without amino acids [Research Institute for the Functional Peptides, Yamagata, Japan] and DMEM/F12 without lysine and arginine [Research Institute for the Functional Peptides and GMEP Cell technologies, Fukuoka, Japan]). Amino acids were purchased from Sigma-Aldrich. Human NSPCs were purchased from Lonza (Basel, Switzerland). HEK293T and HEK293GP cells were cultured in high glucose DMEM (Thermo Fisher Scientific) containing 10% fetal bovine serum (FBS) and 5% penicillin/streptomycin at 37 °C and 5% CO_2 in a humidified incubator. These cell lines were maintained by passaging every 3–4 days.

Constructs
The pLJM1-EGFP-Gal3, pLJM1-mCherry-LAMP1, pLJM1-mCherry and FUGW-Tq-Ca-FLITS constructs were generated by subcloning the EGFP-Gal3, mCherry-LAMP1, mCherry or Tq-Ca-FLITS from pEGFP-Gal3, mCherry-Lysosomes-20 or FHL-cpmTq2-Calcium-lifetime-sensor (pEGFP-hGal3 was a gift from Tamotsu Yoshimori [Addgene plasmid No. 73080; http://n2t.net/addgene:73080; RRID:Addgene_73080][59], mCherry-Lysosomes-20 was a gift from Michael Davidson [Addgene plasmid No. 55073; http://n2t.net/addgene:55073; RRID:Addgene_55073] and FHL-cpmTq2-Calcium-lifetime-sensor was a gift from Dorus Gadella [Addgene plasmid No. 129628; http://n2t.net/addgene:129628; RRID:Addgene_129628][29]) into the pLJM1 or pFUGW lentiviral vector (pLJM1-Empty was a gift from Joshua Mendell [Addgene plasmid No. 91980; http://n2t.net/addgene:91980; RRID: Addgene_91980] and pFUGW-FIRE-pHLy was a gift from Aimee Kao [Addgene plasmid No. 170774; http://n2t.net/addgene:170774; RRID:Addgene_170774][60]). pLenti PGK Blast V5-LUC (w528-1) was a gift from Eric Campeau and Paul Kaufman [Addgene plasmid No. 19166; http://n2t.net/addgene:19166; RRID: Addgene_19166][61]. Full-length human *TFE3 and PPARGC1A* expression constructs were generated by subcloning the cDNAs from TGS04 GBM cells into the pLJM1 lentiviral vector. A full-length human *MGMT* expression construct was generated by subcloning the cDNA from *MGMT*-expressing GBM cells into the pLJM1 lentiviral vector in which a CMV promoter was exchanged for an EF1 promoter from lentiGuide-Puro (lentiGuide-Puro was a gift from Feng Zhang [Addgene plasmid No. 52963; http://n2t.net/addgene:52963; RRID:Addgene_52963][62]). The pLJM1-TFE3-EGFP construct was generated by subcloning the TFE3-*EGFP* from pEGFP-N1-TFE3 (pEGFP-N1-TFE3 was a gift from Shawn Ferguson [Addgene plasmid No. 38120; http://n2t.net/addgene:38120; RRID:Addgene_38120][63]) into the pLJM1 lentiviral vector. Single guide (sg) RNA constructs against human sequences were generated by ligation of annealing oligonucleotides into the BsmBI site of the plentiCRISPR-v2 vector (lentiCRISPR v2 was a gift from Feng Zhang [Addgene plasmid No. 52961][62]). The following *TFE3, TFEB*, and control target sequences for sgRNA (Thermo Fisher Scientific) were used: sgTFE3-1 (ACTGGGGAAGGGAGCCGCGG), sgTFE3-2 (GCTGGGGAGCTGCAGTCCTG), sg-TFEB-1 (GCAGCAGTCGCAGCATCAGA), sg-TFEB-2 (GCTGCTGCAGGGACGTGCGC), sg-control-1 (GAATCATACGTGTCGAAATG), and sg-control-2 (GCTAGTTCAGCGACTATCGC)[64]. The following *TFE3, PPARGC1A* and *MGMT* PCR primers (Thermo Fisher Scientific) were used: *TFE3* (forward: AGAGATATCGCCACCATGGCAGTGCTAGCTCCATGGCTTA, reverse: TTCGTCGACCCTTCTC-CAGCCTTCTCCTT), *PPARGC1A* (forward: CGCACGCGTACCGGTCGCCACCATGGCGTGGGACATG, reverse: CTAACGCGTATGTTACCTGCGCAAGCTTC), *MGMT* (forward: CGCGAATTCACCGGTCGCCACCATGGACAAGGATTG, reverse: TCCGAATTCACATACTCAGTTTCGGCC).

Lentiviral and retroviral infection
For lentiviral vector transfection, HEK293T cells were co-transfected with the lentiviral vector and the packaging vectors (psPAX2 and pVSV-G) at a 1:1:0.5 ratio for the production of the lentivirus. Co-transfection was performed using X-tremeGENE™ HP (Sigma-Aldrich). The culture medium was replaced with NSPC medium at 1-day post-transfection. For retroviral vector transfection, HEK293GP cells were co-transfected with the retroviral vector and pVSV-G at a 1:0.4 ratio for the production of retrovirus. Lentivirus or retrovirus was collected after 48 h and filtered through a 0.45 μm filter. For the transduction, GBM cell lines were infected with lentiviral or retroviral particles suspended in an NSPC medium in the presence of 2 μg/mL polybrene (Sigma-Aldrich). The selection of lentivirus- or retrovirus-infected cells was performed using 0.2 μM puromycin (InvivoGen, San Diego, CA, USA) or 2.5 μM blasticidin (InvivoGen), respectively.

Lysosomal pH assay
Lysosome pH was detected using a Lysosomal Acidic pH Detection kit (Dojindo, Japan). 5×10^4 GBM cells were stained with LysoPrime Green for 30 min and pHLys Red for 30 min and washed with PBS twice. The stained cells were resuspended in 3%FBS/PBS. To generate a standard curve of lysosomal pH, pH calibration buffers and procedures were based on a previous study[60]. The GBM cells stained with LysoPrime Green and pHLys Red were incubated in 100 μL of each pH titration buffer supplemented with 10 μM nigericin and 1× monensin and incubated at 37 °C for 10 min, fluorescence intensity was measured by FACSAriaIII flow cytometry (BD Biosciences). The cells were gated in an SSC-A and FSC-A dot plot and then gated in an FSC-H and FSC-W dot plot to eliminate doublets. (Supplementary Fig. 11A-G). After LysoPrime Green and pHLys Red intensity values were obtained, lysosomal pH of Lyso-low and Lyso-high GBM cell lines was calculated by pHLys Red/ LysoPrime Green values based on the generated standard curve.

Lysosomal proteolytic activity assay
GBM spheroids were collected and dissociated with accutase. GBM cells (1×10^5) were washed and cultured in complete medium or single amino acid depletion NSPC medium for 16–24 h. Cells were dissociated and incubated with 10 μg/mL DQ-BSA (Thermo Fisher Scientific) in 500 μL complete NSPC medium or single amino acid depletion NSPC medium at 37 °C for 4 h. Fluorescence intensity was measured by confocal fluorescence microscopy, Leica DMi8 (Leica Microsystems, Wetzlar, Germany) after the cells had attached to a laminin-coated (0.1 mg/mL) 96-well glass-bottom microplate (Corning), or directly by flow cytometry (BD Biosciences, San Jose, CA, USA). The lysosomal proteolytic activity of GBM cells was detected after treatment of the Nor-NOHA (Cayman), NOC-18 (DOJINDO), homoarginine (Fujifilm Wako Chemicals), and arginine (Sigma). For additional CD44 staining, DQ-BSA-treated cells were dissociated and stained with fluorescently labeled anti-CD44 antibodies (FITC-, APC/Cy7-, or APC-labeled anti-mouse/human CD44 antibodies (103005, lot: B390650; 103027, lot: B381329, and 103011, lot: B371500; BioLegend)) for 1 h on ice. Fluorescence intensity was measured using flow cytometry and/or confocal fluorescence microscopy after CD44-high and -low cells (highest or lowest 15% of total) were separated on a FACSARIA III fluorescence-activated cell sorter (BD Biosciences). The cells were gated in an SSC-A and FSC-A dot plot and then gated in an FSC-H and FSC-W dot plot to eliminate doublets (Supplementary Fig. 12A). For Cathepsin B activity assay, after treatment of indicated drugs, 5×10^4 GBM cells were stained with 1× Rhodamine 110 Cathepsin B substrate reagent (Bio-Rad) for 1 h at 37 °C. The cells were washed with PBS and resuspended in 3%FBS/PBS. Fluorescence intensity was measured by FACSLyric and FACSAriaIII flow cytometry (BD Biosciences).

Mitochondrial reactive oxygen species
GBM cells (1×10^5) were dissociated with accutase and washed in phosphate-buffered saline (PBS). Samples were stained with 2.5 μM MitoSox-Red (Thermo Fisher Scientific) for 15 min at 37 °C and washed twice in 3% FBS/PBS. The cells were gated in an SSC-A and FSC-A dot plot and then gated in an FSC-H and FSC-W dot plot to eliminate

doublets (Supplementary Fig. 12A). The fluorescence intensity was detected on a FACSLyric *flow cytometry* (BD Biosciences).

LysoTracker assay

GBM cells (5000 cells) were seeded into the laminin-coated plate and cultured at 37 °C for 16–24 h. Cells were stained with 60 nM LysoTracker-red (Thermo Fisher Scientific) at 37 °C for 30 min and then stained with 10 µg/mL Hoechst 33342 at 37 °C for 10 min, after the medium was replaced with fresh NSPC medium. Fluorescence was detected after 30 min of drug treatment on a Leica DMi8 confocal fluorescence microscope. Data quantification was performed using LAS X software (Leica Microsystems).

Galectin-3 puncta assay

GBM cells were generated to stably express EGFP-Gal3 by lentiviral transduction. GBM cells (5000 cells) were seeded onto a laminin-coated 96-well glass-bottom microplate and cultured in complete NSPC medium or lysine-depleted NSPC medium at 37 °C for 16–24 h; the cells were then treated with DMSO or the indicated drugs for 15 min. Cells were stained with 10 µg/mL Hoechst 33342 at 37 °C for 10 min. Galectin-3-positive puncta were imaged at 40× magnification (using an objective water immersion lens) on a Leica DMi8 confocal fluorescence microscope. Quantitative data analysis was performed using LAS X software.

Sphere formation assay

GBM spheroids were dissociated with accutase, and washed with complete NSPC medium or lysine-depleted NSPC medium three times. GBM cells (500-1000 cells) were seeded in a complete NSPC medium or lysine-depleted NSPC medium containing 1% methylcellulose (Fujifilm Wako Chemicals) with and without drugs. Irradiation was performed with MBR-1520R-3 (HITACHI, Ibaraki, Japan). The number and size of GBM spheres were automatically evaluated after 10–14 days of culture in an ultra-low attachment 96-well plate (Corning) using a Keyence BZ-9000 fluorescence microscope (Keyence, Osaka, *Japan*). The dissociated CD44-high or -low cells were stained with fluorescently labeled anti-CD44 antibodies (FITC-, APC/Cy7-, or APC-labeled anti-mouse/human CD44 antibodies) for 1 h on ice. CD44-high and -low cells were separated on FACSARIA III fluorescence-activated cell sorter (BD Biosciences). The cells were gated in an SSC-A and FSC-A dot plot and then gated in an FSC-H and FSC-W dot plot to eliminate doublets (Supplementary Fig. 12B, C).

Bioluminescence imaging

Patient-derived GBM cells were infected with the retrovirus from the pBabe retrovirus vector containing firefly luciferase. Intracranial transplantation was performed on anesthetized 4-week-old female Balb/c nu/nu mice, using luciferase-expressing GBM cells (1×10^5/mouse). Bioluminescence was confirmed following the intraperitoneal injection of D-Luciferin (150 mg/kg) and imaging on an IVIS Lumina III imaging system (PerkinElmer, Waltham, MA, USA).

Immunoblotting

GBM cells were lysed with RIPA buffer (50 mmol/L Tris-HCl, pH 8.0, 150 mM sodium chloride, 1% NP-40, 0.5% sodium deoxycholate, 0.1% sodium dodecyl sulfate, and 2 mM EDTA) containing 1 mM PMSF protease inhibitor. The lysates were then centrifuged at $14,000 \times g$ at 4 °C for 10 min. Quantification of protein concentration was performed using a BCA Protein Assay Kit (Thermo Fisher Scientific). 5 µg protein samples were separated on a 10% or 15% SDS-PAGE and transferred to 0.45 µm PVDF membranes (Millipore, Billerica, MA, USA). Membranes were blocked with 5% skimmed milk (BD Biosciences) in tris-buffered saline with Tween 20 (TBST) after protein transfer. Membranes were then probed with primary antibodies, and diluted in Can Get Signal Solution (TOYOBO, Osaka, Japan), at 4 °C for 16–24 h. The membranes were incubated with secondary antibodies at

room temperature for 1 h. Protein detection was performed using ECL Prime (GE Healthcare, Piscataway, NJ, USA). The following antibodies were used: anti-TFE3 (Sigma-Aldrich, HPA023881; Lot: 000014969; 1:1000), anti-TFEB (Cell Signaling Technologies, Danvers, MA, USA, 4240s; Lot: 3; 1:1000), anti-cathepsin C (Santa Cruz, sc-74590; Lot: 2030 1:1000), anti-PTEN (Cell Signaling Technologies, 9559S; Lot: 12; 1:1000), anti-AKT (Cell Signaling Technologies, 4685S; Lot: 3; 1:1000), anti-Phospho-Akt (Ser473) (Cell Signaling Technologies, 4060S; Lot: 14l; 1:1000), anti-p44/42 MAPK (Erk1/2) (Cell Signaling Technologies, 4695S; Lot: 14; 1:1000), anti-Phospho-p44/42 MAPK (Erk1/2) (Cell Signaling Technologies, 9101S; Lot: 28; 1:1000); anti-vinculin (Sigma-Aldrich, 700062; Lot: 1999930; 1:1500) and anti-*β*-actin (Sigma-Aldrich, A5441; Lot: 0000090942; 1:2000).

RNA-sequencing and data analysis

RNA samples were extracted from patient-derived GBM cells by RNeasy Mini Kit (QIAGEN, Hilden, Germany), and bulk RNA sequencing was performed as described previously[65]. The libraries for sequencing were constructed using TruSeq Stranded mRNA (Illumina, San Diego, CA, USA). The average size of the libraries was 326–356 bp. High-throughput sequencing of the samples was performed using the NextSeq 500/550 High Output Kit v2.5 (Illumina, 75 cycles pair-end, 40/40 cycles). The bulk-RNA-sequencing results were analyzed using the CLC Genomics Workbench Version 12.0.2 (Filgen Inc., Aichi, Japan). RNA-sequencing data were processed and analyzed using Gene set enrichment analysis software by following the guidelines[66]. The differential analysis of count data between Lyso-high and Lyso-low GBM cells was performed using Deseq2 in the R bioconductor package. Gene-ontology analysis for upregulated genes was conducted using clustertProfiler, supplied as an R package (https://bioconductor.org/packages/release/bioc/html/clusterProfiler.html).

Calcium detection assay

For Fluo-4 staining, 3×10^4 GBM cells were seeded on a laminin-coated 48-well plate. The cells were stained with Fluo-4 (Thermo Fisher Scientific) at 37 °C for 30 min and at room temperature for 30 min after culture for 16–24 h. The cells were washed in KRB calcium-free buffer (Millipore). The fluorescence intensity was detected by FACS or microscope For Rhod-3 staining, 1×10^4 GBM cells were seeded on a laminin-coated 96-well glass-bottom plate. The cells were stained with Rhod-3 following the manufacturer's protocol (ThermoFisher). The fluorescence intensity of Rhod-3 was imaged and quantified using a Leica DMi8 confocal fluorescence microscope.

Measurement of intracellular calcium (Ca²⁺) concentration by fluorescence lifetime imaging microscopy (FLIM)

For imaging, GBM cells expressing Tq-Ca-FLITS were seeded at a density of 0.75×10^5 cells on poly-L-lysine-coated glass-bottom dishes. FLIM was performed using an FV1200 confocal microscope (Olympus) equipped with a rapidFLIM^HiRes and a MultiHarp 150 Time-Correlated Single Photon Counting (TCSPC) unit from PicoQuant. Tq-Ca-FLITS was excited with a 440 nm pulse laser (PicoQuant), and fluorescence emission was collected through a 483/40 nm bandpass filter (Semrock). Fluorescence lifetime values were calculated using SymPhoTime 64 software (PicoQuant). The fluorescence lifetime decay histogram was fitted with a two-exponential function, with the arrival time fixed at 0–8 ns starting from the pulse laser[67]. The intensity-weighted average lifetime was then reported. To estimate intracellular Ca²⁺ concentration, permeabilized GBM cells were used for in-cell calibration. First, GBM cells expressing Tq-Ca-FLITS were permeabilized with 150 µM β-escin in a solution containing 20 mM HEPES, 140 mM KCl, 10 mM NaCl, and 1 mM MgCl₂ (pH 7.2)[68]. After 4 min of treatment, cells were washed twice with PBS. Next, Tq-Ca-FLITS expressed in permeabilized GBM cells was calibrated using the Calcium Calibration Buffer Kit No. 1 (C3008MP, ThermoFisher) in the presence of 3 µM ionomycin and

3 µM thapsigargin. The fluorescence lifetime was plotted against Ca^{2+} concentration, and the curve was fitted using the Hill equation in Origin Software (OriginPro, Version 2022b). This calibration curve was then used to calculate the intracellular Ca^{2+} concentration.

Mutation detection assay

To detect EGFRvIII and IDH1R132 mutations in KGS03, KGS04, KGS22, KGS10, KGS23, TGS04, total RNA of GBM cell lines was extracted and reverse-transcribed into cDNA by using the Advantage RT-for-PCR following the manufacturer's protocol (Takara Bio). The region spanning EGFR exon 1 and exon 8 was then amplified by PCR. EGFRvIII (128 bp) or WT EGFR (929 bp) were visualized by 2% agarose gel electrophoresis[69]. The IDH1R132 region was amplified by PCR and the amplified fragment was sequenced. The following primers were used: EGFR-exon1: GGGCTCTGGGAGGAAAAGAAA EGFR-exon8: AGGCCCTT CGCACTTCTTAC, IDH1-F: AGAATCGTGATGCCACCAACGACCAAG, IDH1-R: CTTGTAAGGGGATCCTATTGTGCAGCC. The sensitivity of GBM cell lines to nutlin-3 (5 µM) was assessed to detect WT p53 using a sphere formation assay.

Mitochondrial membrane potential assay

Cells were incubated with JC-10 dye buffer (Abcam plc, Cambridge, UK) for 30 min at 37 °C in 5% CO_2. The mitochondrial membrane potential of GBM cell lines was measured by FACSLyric *flow cytometry* based on the accumulation of JC-10 fluorescence. The cells were gated in an SSC-A and FSC-A dot plot and then gated in an FSC-H and FSC-W dot plot to eliminate doublets (Supplementary Fig. 12D, 13A).

Mitochondrial stress assay

Oxygen consumption was measured at 37 °C using an XFe-24 analyzer (Seahorse Bioscience Inc., North Billerica, MA, USA). GBM cells (5×10^4) were resuspended in NSPC medium, seeded in cell-tak (Corning)-coated 24-well plates, and incubated at 37 °C for 1 h. NSPC medium was replaced with unbuffered DMEM containing 5 mM glucose and 1 mM pyruvate and the cells were reintubated at 37 °C without CO_2 addition for 1 h. The following substrates were added: oligomycin (1.5 µM), FCCP (0.5 µM), and antimycin A/Rotenone (0.5 µM). The data for each time point represent an average of those from five different wells.

Immunohistochemistry

Tissue sections from GBM patients were treated with target retrieval solution (Dako) and incubated with a primary antibody recognizing TFE3 (1:100) overnight at 4 °C, after the blocking with 5% BSA in PBS. The tissue sections were then washed in PBS and visualized using an HRP-conjugated secondary antibody (GE Healthcare) and the DAB Peroxidase Substrate Kit (Vector Laboratories, Burlingame, CA, USA). Immunostained sections were counterstained with hematoxylin and viewed on a Keyence BZ-X810 microscope (Keyence). The number of the TFE3-positive GBM cells in the acquired images was counted automatically by ImageJ software.

Immunofluorescence

Cells sorted by CD44 levels were attached on a glass slide by cytospin and treated with 3.7% paraformaldehyde for 15 min at room temperature. After washing with PBS, the cells were treated with 0.3% Triton X-100/PBS with 0.05% Tween 20 for 5 min. After blocking with 1% BSA/PBS with 0.05% Tween 20, the cells were incubated with a primary antibody recognizing TFE3 (HPA023881, Sigma-Aldrich) (1:100) overnight at 4 °C. The cells were then washed in PBS and visualized using an Alexa Fluor® 488-conjugated secondary antibody (Thermo Fisher Scientific). Immunostained cells were mounted with ProLong® Diamond with DAPI (Thermo Fisher Scientific) and viewed on a Leica DMi8 confocal fluorescence microscope. The mean fluorescence intensity (MFI) of nuclear TFE3 in the acquired images was calculated automatically by ImageJ software.

Metabolome analysis

For capillary electrophoresis Time-of-flight mass spectrometer (CE-TOFMS) analysis, patient-derived GBM cells with low or high lysosomal activity ($n = 3$ biological replicates each) were washed with 5% mannitol and lysed in methanol (1 mL) containing 25 µM internal standards (L-methionine sulfone (Wako), 2-morpholinoethanesulfonic acid, mono-hydrate (MES) (DOJINDO, Kumamoto, Japan), D-camphor-10-sulfonic acid sodium salt (CSA) (Fujifilm Wako Chemicals)). After homogenization, 400 µL of the sample was mixed with 400 µL chloroform and 200 µL Milli-Q water, followed by centrifugation ($10,000 \times g$, 4 °C, 3 min). The upper aqueous layer (400 µL) was filtered using a 5-kDa cutoff filter (Human Metabolome Technologies, Tsuruoka, Japan) to remove proteins, lyophilized, and reconstituted in 25 µL Milli-Q water with 200 µM reference compounds (3-aminopyrrolidine [Aldric] and trimesate [Wako]) for CE-TOFMS analysis.

CE-TOFMS experiments were performed on an Agilent CE system (Agilent Technologies, Waldbronn, Germany) coupled with an Agilent G6230B LC/MSD TOF system (Agilent Technologies, Palo Alto, CA, USA), an Agilent1260 Infinity 2 series binary HPLC pump, and the G1603A Agilent CE-MS adapter- and G1607A Agilent CE-ESI-MS sprayer kit., using MassHunter software (B.08.00) for control and data acquisition. For cationic metabolites, a fused silica capillary (50 µm i.d. × 100 cm) with 1 M formic acid as the electrolyte was used[70]. The sample (5 µL) was injected at 50 mbar for 5 s with 30 kV applied voltage. The capillary was maintained at 20 °C and the sample tray was below 5 °C. Methanol/water (50% v/v) containing 0.01 µM hexakis (2,2-difluoroethoxy) phosphazene was delivered as the sheath liquid at 10 µL/min. ESI-TOFMS was performed in positive ion mode with 4 kV capillary voltage and at 7 psig flow rate of heated dry nitrogen gas (heater temperature 300 °C). The fragmentor, skimmer, and Oct RFV voltage were set at 75 V, 50 V, and 500 V, respectively. Each acquired spectrum was automatically recalibrated using the masses of the reference standards (^{13}C isotopic ion of a protonated methanol dimer, m/z 66.0631) and (protonated ion of hexakis (2,2-difluoroethoxy) phosphazene, m/z 622.0290). To identify metabolites, relative migration times were calculated by normalization to the reference compound 3-aminopyrrolidine. Quantification was performed by comparing peak areas to calibration curves generated using internal standardization techniques with methionine sulfone[71].

For anionic metabolites, a COSMO (+) capillary (50 µm i.d. × 105 cm) (Nacalai Tesque, Kyoto, Japan) with 50 mM ammonium acetate (pH 8.5) as the electrolyte was used. The sample (30 nL) was injected at 50 mbar for 30 s with −30 kV applied voltage. Methanol/5 mM ammonium acetate (50% v/v) containing 0.01 µM hexakis (2,2-difluoroethoxy) phosphazene was delivered as the sheath liquid at 10 µL/min. The platinum needle was used for anionic metabolite analysis[72]. ESI-TOFMS was performed in negative ion mode with 3.5 kV capillary voltage. The fragmentor, skimmer, and Oct RFV voltage were set at 100 V, 50 V, and 500 V, respectively. Each acquired spectrum was automatically recalibrated using the masses of the reference standards (^{13}C isotopic ion of deprotonated acetic acid dimer, m/z 120.0383) and (hexakis (2,2-difluoroethoxy) phosphazene + deprotonated acetic acid, m/z 680.0355). For anion analysis, trimesate and CAS were used as the reference and the internal standards, respectively. Data analysis was conducted with our proprietary software (MasterHands (ver. 2.17.0.10)) and MetaboAnalyst 5.0[73].

Nitric oxide detection assay

GBM cells were treated with NOC-18 (DOJINDO), 25 mM arginine, or preincubated with lysine-depleted NSPC medium for 16–24 h at 37 °C. The nitric oxide levels were then measured by FACSLyric *flow cytometry* based on the accumulation of DAF-FM DA (Goryo chemical, Hokkaido, Japan). The cells were gated in an SSC-A and FSC-A dot plot and then gated in an FSC-H and FSC-W dot plot to eliminate doublets (Supplementary Fig. 13B−D).

Drug screening

Libraries used for drug screening were the SCADS inhibitor kits (Molecular Profiling Committee, Grant-in-Aid for Scientific Research on Innovative Areas "Advanced Animal Model Support (AdAMS)" from The Ministry of Education, Culture, Sports, Science and Technology, Japan (KAKENHI 16H06276)). The TGS04 cells were pretreated with or without homoarginine 20 mM and seeded into the 96-well plates (7500 cells/well), then cultured with library compounds ($0.001\,\mu M$, $0.005\,\mu M$, $0.02\,\mu M$, $0.1\,\mu M$, $0.5\,\mu M$, $2\,\mu M$, $10\,\mu M$) (Supplementary Table 1). The cell viability was measured after 48 h. The "Index of drug sensitivity" was calculated as the ratio of value 2/value 1 at each dose of a compound, where value 1 was the cell viability (%) in TGS04 cells pretreated with 20 mM homoarginine and value 2 was the cell viability (%) in TGS04 cells without pretreatment of homoarginine.

Apoptosis detection assay

Cells (1×10^5) were treated with indicated drugs for 16–24 h. After dissociation, the cells were washed in 3% FBS/PBS (−) and then incubated in Annexin V binding buffer (BD Biosciences) containing $2.5\,\mu L$ Annexin V-FITC (BD Biosciences) and 7-AAD (BD Biosciences) for 15 min at room temperature. Fluorescence intensity was measured by FACSAriaIII flow cytometry (BD Biosciences).

Patient-derived xenograft mouse model

Four-week-old female BALB/c nu/nu mice (Sankyo Labo Service Corporation, INC. Japan) were anesthetized and placed into a stereotactic apparatus equipped with a z-axis (Stoelting). A small hole was bored into the skull 0.5 mm anterior and 3.0 mm lateral to bregma using a dental drill. Human patient-derived GBM cells (1×10^5/mouse) were injected into the right striatum 3 mm below the surface of the brain using a 10 mL Hamilton syringe with a 26-gauge needle. The scalp was closed using an Autoclip Applier. Animals were monitored daily for neurologic deficits. The animals were housed under SPF conditions in groups of five mice per cage and maintained in a temperature-controlled ($23 \pm 2\,°C$) and humidity-regulated environment ($30 \sim 70\%$) with a 12-h light/dark cycle. They had free access to standard food (CRF1 (Oriental Yeast, Tokyo)) and water. All animal experiments were approved by the Committee on Animal Experimentation of Kanazawa University and performed following the university's guidelines for the care and use of laboratory animals. For the detection of the synergistic effect of TMZ and homoarginine, mice were randomly divided into four groups (5 mice per group) and treated with: (1) DMSO (control); (2) TMZ (1.5 mg/kg) dissolved in DMSO; (3) homoarginine (Fujifilm Wako Chemicals) (200 mg/kg) dissolved in PBS; (4) homoarginine plus TMZ. Homoarginine was pretreated for 7 days before 7 day's treatment of TMZ. All drugs were intraperitoneally injected into mice.

Statistics and reproducibility

No data were excluded from the analyses. Data entry and analyses were performed in a blinded fashion. Mice were randomly assigned for in vivo experiments. Unpaired two-tailed Student's t-tests were used to compare two groups. Two-way analysis of variance (ANOVA) was used to compare more than two groups. The statistical significance of differences between survival rates was determined using the log-rank test. To evaluate differences in lysosomal proteolytic activity and actual calcium level across groups, a nested t-test was performed. Significance calculations were performed using GraphPad Prism software 8.0 (GraphPad Software, San Diego, CA, USA). The results are considered significant when $P < 0.05$. ns, not significant; $****P < 0.0001$. All the experiments were repeated two or more times with similar results.

Reporting summary

Further information on research design is available in the Nature Portfolio Reporting Summary linked to this article.

Data availability

All data associated with this study are presented in the paper, source data file, or the Supplementary Materials. The TFE3 targets were downloaded from ChipBase. All RNA-sequencing data were deposited in gene expression omnibus (GEO) under accession number GSE230826. The metabolome data were deposited in MetaboBank under accession number MTBKS256. Source data are provided with this paper.

References

1. Ochocki, J. D. & Simon, M. C. Nutrient-sensing pathways and metabolic regulation in stem cells. *J. Cell Biol.* **203**, 23–33 (2013).
2. Altea-Manzano, P., Cuadros, A. M., Broadfield, L. A. & Fendt, S. M. Nutrient metabolism and cancer in the in vivo context: a metabolic game of give and take. *EMBO Rep.* **21**, e50635 (2020).
3. Vander Heiden, M. G. & DeBerardinis, R. J. Understanding the intersections between metabolism and cancer biology. *Cell* **168**, 657–669 (2017).
4. Buck, M. D. et al. Mitochondrial dynamics controls T cell fate through metabolic programming. *Cell* **166**, 63–76 (2016).
5. Gordaliza-Alaguero, I., Cantó, C. & Zorzano, A. Metabolic implications of organelle-mitochondria communication. *EMBO Rep.* **20**, e47928 (2019).
6. Miller, D. R. & Thorburn, A. Autophagy and organelle homeostasis in cancer. *Dev. Cell* **56**, 906–918 (2021).
7. Porporato, P. E., Filigheddu, N., Pedro, J. M. B.-S., Kroemer, G. & Galluzzi, L. Mitochondrial metabolism and cancer. *Cell Res.* **28**, 265–280 (2018).
8. Vasan, K., Werner, M. & Chandel, N. S. Mitochondrial metabolism as a target for cancer therapy. *Cell Metab.* **32**, 341–352 (2020).
9. Bonam, S. R., Wang, F. & Muller, S. Lysosomes as a therapeutic target. *Nat. Rev. Drug Discov.* **18**, 923–948 (2019).
10. Appelqvist, H., Wäster, P., Kågedal, K. & Öllinger, K. The lysosome: from waste bag to potential therapeutic target. *J. Mol. Cell Biol.* **5**, 214–226 (2013).
11. Perera, R. M. & Zoncu, R. The lysosome as a regulatory hub. *Annu. Rev. Cell Dev. Biol.* **32**, 223–253 (2016).
12. Bonifacino, J. S. & Neefjes, J. Moving and positioning the endolysosomal system. *Curr. Opin. Cell Biol.* **47**, 1–8 (2017).
13. Wong, Y. C., Peng, W. & Krainc, D. Lysosomal regulation of inter-mitochondrial contact fate and motility in Charcot-Marie-tooth type 2. *Dev. Cell* **50**, 339–354.e334 (2019).
14. Napolitano, G. & Ballabio, A. TFEB at a glance. *J. Cell Sci.* **129**, 2475–2481 (2016).
15. Perera, R. M. et al. Transcriptional control of autophagy-lysosome function drives pancreatic cancer metabolism. *Nature* **524**, 361–365 (2015).
16. Zhu, X. et al. TFEB promotes prostate cancer progression via regulating ABCA2-dependent lysosomal biogenesis. *Front. Oncol.* **11**, 632524 (2021).
17. Garraway, L. A. et al. Integrative genomic analyses identify MITF as a lineage survival oncogene amplified in malignant melanoma. *Nature* **436**, 117–122 (2005).
18. Davis, M. E. Glioblastoma: overview of disease and treatment. *Clin. J. Oncol. Nurs.* **20**, S2–S8 (2016).
19. Ou, A., Yung, W. K. A. & Majd, N. Molecular mechanisms of treatment resistance in glioblastoma. *Int. J. Mol. Sci.* **22**, 351–374 (2021).
20. Osuka, S. & Van Meir, E. G. Overcoming therapeutic resistance in glioblastoma: the way forward. *J. Clin. Invest* **127**, 415–426 (2017).
21. Dymova, M. A., Kuligina, E. V. & Richter, V. A. Molecular mechanisms of drug resistance in glioblastoma. *Int. J. Mol. Sci.* **22**, 6385–6399 (2021).
22. St-Coeur, P. D., Poitras, J. J., Cuperlovic-Culf, M., Touaibia, M. & Morin, P. Jr. Investigating a signature of temozolomide resistance in

GBM cell lines using metabolomics. *J. Neurooncol.* **125**, 91–102 (2015).

23. Yuan, H. et al. Lysine catabolism reprograms tumour immunity through histone crotonylation. *Nature* **617**, 818–826 (2023).

24. Tang, T. et al. The role of lysosomes in cancer development and progression. *Cell Biosci.* **10**, 131 (2020).

25. Kanzawa, T. et al. Role of autophagy in temozolomide-induced cytotoxicity for malignant glioma cells. *Cell Death Differ.* **11**, 448–457 (2004).

26. Yang, J. H., Li, J. H., Jiang, S., Zhou, H. & Qu, L. H. ChIPBase: a database for decoding the transcriptional regulation of long non-coding RNA and microRNA genes from ChIP-Seq data. *Nucleic Acids Res.* **41**, D177–D187 (2013).

27. Zhou, K. R. et al. ChIPBase v2.0: decoding transcriptional regulatory networks of non-coding RNAs and protein-coding genes from ChIP-seq data. *Nucleic Acids Res.* **45**, D43–d50 (2017).

28. De Vitto, H., Bode, A. M. & Dong, Z. The PGC-1/ERR network and its role in precision oncology. *NPJ Precis Oncol.* **3**, 9 (2019).

29. van der Linden, F. H. et al. A turquoise fluorescence lifetime-based biosensor for quantitative imaging of intracellular calcium. *Nat. Commun.* **12**, 7159 (2021).

30. Yoon, M. S. The emerging role of branched-chain amino acids in insulin resistance and metabolism. *Nutrients* **8**, 405–417 (2016).

31. Bihuniak, J. D. & Insogna, K. L. The effects of dietary protein and amino acids on skeletal metabolism. *Mol. Cell. Endocrinol.* **410**, 78–86 (2015).

32. Hsu, C. C. et al. Lysine deprivation induces AKT-AADAT signaling and overcomes EGFR-TKIs resistance in EGFR-mutant non-small cell lung cancer cells. *Cancers* **13**, 272–288 (2021).

33. Lee, L. M.-Y. et al. Lysine deprivation suppresses adipogenesis in 3T3-L1 cells: a transcriptome analysis. *Int. J. Mol. Sci.* **24**, 9402 (2023).

34. Griffith, R. S., DeLong, D. C. & Nelson, J. D. Relation of arginine-lysine antagonism to herpes simplex growth in tissue culture. *Chemotherapy* **27**, 209–213 (1981).

35. Rotoli, B. M., Barilli, A., Visigalli, R., Ferrari, F. & Dall'Asta, V. y+LAT1 and y+LAT2 contribution to arginine uptake in different human cell models: implications in the pathophysiology of lysinuric protein intolerance. *J. Cell Mol. Med.* **24**, 921–929 (2020).

36. Jungnickel, K. E. J., Parker, J. L. & Newstead, S. Structural basis for amino acid transport by the CAT family of SLC7 transporters. *Nat. Commun.* **9**, 550 (2018).

37. Liaudet, L. et al. Effect of L-lysine on nitric oxide overproduction in endotoxic shock. *Br. J. Pharmacol.* **122**, 742–748 (1997).

38. Böger, R. H. The pharmacodynamics of L-arginine. *J. Nutr.* **137**, 1650s–1655s (2007).

39. Lee, J., Ryu, H., Ferrante, R. J., Morris, S. M. Jr. & Ratan, R. R. Translational control of inducible nitric oxide synthase expression by arginine can explain the arginine paradox. *Proc. Natl Acad. Sci. USA* **100**, 4843–4848 (2003).

40. Jiang, L. et al. Lysosomal nitric oxide determines transition from autophagy to ferroptosis after exposure to plasma-activated Ringer's lactate. *Redox Biol.* **43**, 101989 (2021).

41. Martínez-Garay, C. & Djouder, N. Dietary interventions and precision nutrition in cancer therapy. *Trends Mol. Med.* **29**, 489–511 (2023).

42. Morita, M., Kudo, K., Shima, H. & Tanuma, N. Dietary intervention as a therapeutic for cancer. *Cancer Sci.* **112**, 498–504 (2021).

43. Tajan, M. & Vousden, K. H. Dietary approaches to cancer therapy. *Cancer Cell* **37**, 767–785 (2020).

44. Moali, C., Boucher, J. L., Sari, M. A., Stuehr, D. J. & Mansuy, D. Substrate specificity of NO synthases: detailed comparison of L-arginine, homo-L-arginine, their N omega-hydroxy derivatives, and N omega-hydroxynor-L-arginine. *Biochemistry* **37**, 10453–10460 (1998).

45. Zhang, X. et al. Nitric oxide inhibits autophagy and promotes apoptosis in hepatocellular carcinoma. *Cancer Sci.* **110**, 1054–1063 (2019).

46. Lynch, M. R. et al. TFEB-driven lysosomal biogenesis is pivotal for PGC1α-dependent renal stress resistance. *JCI Insight* **5**, e126749 (2019).

47. Jing, Y. et al. Therapeutic advantage of targeting lysosomal membrane integrity supported by lysophagy in malignant glioma. *Cancer Sci.* **113**, 2716–2726 (2022).

48. Zhitomirsky, B. & Assaraf, Y. G. Lysosomal sequestration of hydrophobic weak base chemotherapeutics triggers lysosomal biogenesis and lysosome-dependent cancer multidrug resistance. *Oncotarget* **6**, 1143–1156 (2015).

49. Geisslinger, F. et al. Targeting TPC2 sensitizes acute lymphoblastic leukemia cells to chemotherapeutics by impairing lysosomal function. *Cell Death Dis.* **13**, 668 (2022).

50. Yang, E. et al. PTRF/Cavin-1 enhances chemo-resistance and promotes temozolomide efflux through extracellular vesicles in glioblastoma. *Theranostics* **12**, 4330–4347 (2022).

51. Yuizumi, N. et al. Maintenance of neural stem-progenitor cells by the lysosomal biosynthesis regulators TFEB and TFE3 in the embryonic mouse telencephalon. *Stem Cells* **39**, 929–944 (2021).

52. Ravichandran, M. et al. Coordinated transcriptional and catabolic programs support iron-dependent adaptation to RAS-MAPK pathway inhibition in pancreatic cancer. *Cancer Discov.* **12**, 2198–2219 (2022).

53. Nezich, C. L., Wang, C., Fogel, A. I. & Youle, R. J. MiT/TFE transcription factors are activated during mitophagy downstream of Parkin and Atg5. *J. Cell Biol.* **210**, 435–450 (2015).

54. Asrani, K. et al. mTORC1 feedback to AKT modulates lysosomal biogenesis through MiT/TFE regulation. *J. Clin. Invest.* **129**, 5584–5599 (2019).

55. Ikushima, H. et al. Autocrine TGF-beta signaling maintains tumorigenicity of glioma-initiating cells through Sry-related HMG-box factors. *Cell Stem Cell* **5**, 504–514 (2009).

56. Kitabayashi, T. et al. Identification of GSK3β inhibitor kenpaullone as a temozolomide enhancer against glioblastoma. *Sci. Rep.* **9**, 10049 (2019).

57. Wang, Y. et al. COL1A2 inhibition suppresses glioblastoma cell proliferation and invasion. *J. Neurosurg.* **138**, 639–648 (2023).

58. Zhang, G. et al. RBPJ contributes to the malignancy of glioblastoma and induction of proneural-mesenchymal transition via IL-6-STAT3 pathway. *Cancer Sci.* **111**, 4166–4176 (2020).

59. Maejima, I. et al. Autophagy sequesters damaged lysosomes to control lysosomal biogenesis and kidney injury. *EMBO J.* **32**, 2336–2347 (2013).

60. Chin, M. Y. et al. Genetically encoded, pH-sensitive mTFP1 biosensor for probing lysosomal pH. *ACS Sens.* **6**, 2168–2180 (2021).

61. Campeau, E. et al. A versatile viral system for expression and depletion of proteins in mammalian cells. *PLoS ONE* **4**, e6529 (2009).

62. Sanjana, N. E., Shalem, O. & Zhang, F. Improved vectors and genome-wide libraries for CRISPR screening. *Nat. Methods* **11**, 783–784 (2014).

63. Roczniak-Ferguson, A. et al. The transcription factor TFEB links mTORC1 signaling to transcriptional control of lysosome homeostasis. *Sci. Signal.* **5**, ra42 (2012).

64. Park, R. J. et al. A genome-wide CRISPR screen identifies a restricted set of HIV host dependency factors. *Nat. Genet.* **49**, 193–203 (2017).

65. Iwabuchi, S. et al. Immune cells profiles in the different sites of COVID-19-affected lung lobes in a single patient. *Front. Med.* **9**, 841170 (2022).

66. Mootha, V. K. et al. PGC-1alpha-responsive genes involved in oxidative phosphorylation are coordinately downregulated in human diabetes. *Nat. Genet.* **34**, 267–273 (2003).

67. Arai, S. et al. qMaLioffG: a single green fluorescent protein FLIM indicator enabling quantitative imaging of endogenous ATP. Preprint at *bioRxiv* https://doi.org/10.1101/2023.08.29.555275 (2023).

68. Suzuki, J. et al. Imaging intraorganellar Ca2+ at subcellular resolution using CEPIA. *Nat. Commun.* **5**, 4153 (2014).

69. Ji, H. et al. Epidermal growth factor receptor variant III mutations in lung tumorigenesis and sensitivity to tyrosine kinase inhibitors. *Proc. Natl Acad. Sci. USA* **103**, 7817–7822 (2006).

70. Soga, T. et al. Quantitative metabolome analysis using capillary electrophoresis mass spectrometry. *J. Proteome Res.* **2**, 488–494 (2003).

71. Soga, T. et al. Differential metabolomics reveals ophthalmic acid as an oxidative stress biomarker indicating hepatic glutathione consumption. *J. Biol. Chem.* **281**, 16768–16776 (2006).

72. Soga, T. et al. Metabolomic profiling of anionic metabolites by capillary electrophoresis mass spectrometry. *Anal. Chem.* **81**, 6165–6174 (2009).

73. Pang, Z. et al. Using MetaboAnalyst 5.0 for LC-HRMS spectra processing, multi-omics integration and covariate adjustment of global metabolomics data. *Nat. Protoc.* **17**, 1735–1761 (2022).

Author contributions
Y.J., M.K., M.I.S., A.K., M.Z., M.U., Y.T., K.K., X.C., Y.Y., and A.H. conceptualized and discussed the project. Y.J., M.K., M.I.S., H.T.V., H.A., C.V., S.A., S.H., T.S., T.T., and A.H. developed the study plan and designed the experiments. Y.J., M.K., M.I.S., H.S., and S.I. performed the experiments. Y.J., M.K., M.I.S., S.I., and M.N. analyzed the data. M.K. and A.H. administered the project and acquired the funding. Y.J. wrote the original draft. M.K. and A.H. reviewed and edited the manuscript.

Competing interests
The authors declare no competing interests.

Additional information
Supplementary information The online version contains supplementary material available at https://doi.org/10.1038/s41467-025-56946-z.

Correspondence and requests for materials should be addressed to Atsushi Hirao.

Peer review information *Nature Communications* thanks Marja Jäättelä, and the other, anonymous, reviewer(s) for their contribution to the peer review of this work. A peer review file is available.

Reprints and permissions information is available at http://www.nature.com/reprints

Publisher's note Springer Nature remains neutral with regard to jurisdictional claims in published maps and institutional affiliations.

[1]Division of Molecular Genetics, Cancer Research Institute, Kanazawa University, Kanazawa, Ishikawa, Japan. [2]WPI Nano Life Science Institute (WPI-Nano LSI), Kanazawa University, Kanazawa, Ishikawa, Japan. [3]Department of Zoology, Faculty of Science, Minia University, Minia, Egypt. [4]Faculty of Pharmaceutical Sciences, Institute of Medical, Pharmaceutical and Health Sciences, Kanazawa University, Kanazawa, Ishikawa, Japan. [5]Department of Neurosurgery, Graduate School of Medical Science, Kanazawa University, Kanazawa, Ishikawa, Japan. [6]Department of Molecular Pathophysiology, Institute of Advanced Medicine, Wakayama Medical University, Wakayama, Japan. [7]Institute for Frontier Science Initiative, Kanazawa University, Kanazawa, Ishikawa, Japan. [8]Institute for Advanced Biosciences, Keio University, Tsuruoka, Yamagata, Japan. [9]Human Biology-Microbiome-Quantum Research Center (WPI-Bio2Q), Keio University, Tokyo, Japan. [10]Division of Innovative Cancer Therapy, Institute of Medical Science, The University of Tokyo, Tokyo, Japan. [11]Present address: Department of Medical Biology and Genetics, Hanoi Medical University, Ha Noi, Vietnam. [12]These authors contributed equally: Yongwei Jing, Masahiko Kobayashi. ✉e-mail: ahirao@staff.kanazawa-u.ac.jp